AFRL-AFOSR-VA-TR-2018-0365

Nanoelectronics Innervated Cells, Cell Networks and Three-Dimensional Biomaterials

Charles Lieber
HARVARD COLLEGE PRESIDENT & FELLOWS OF

09/04/2018
Final Report

DISTRIBUTION A: Distribution approved for public release.

Air Force Research Laboratory
AF Office Of Scientific Research (AFOSR)/ RTB2
Arlington, Virginia 22203
Air Force Materiel Command

REPORT DOCUMENTATION PAGE

Form Approved
OMB No. 0704-0188

The public reporting burden for this collection of information is estimated to average 1 hour per response, including the time for reviewing instructions, searching existing data sources, gathering and maintaining the data needed, and completing and reviewing the collection of information. Send comments regarding this burden estimate or any other aspect of this collection of information, including suggestions for reducing the burden, to Department of Defense, Executive Services, Directorate (0704-0188). Respondents should be aware that notwithstanding any other provision of law, no person shall be subject to any penalty for failing to comply with a collection of information if it does not display a currently valid OMB control number.
PLEASE DO NOT RETURN YOUR FORM TO THE ABOVE ORGANIZATION.

1. REPORT DATE *(DD-MM-YYYY)*	2. REPORT TYPE	3. DATES COVERED *(From - To)*
03-10-2018	Final Performance	15 Jun 2014 to 31 Oct 2018

4. TITLE AND SUBTITLE
Nanoelectronics Innervated Cells, Cell Networks and Three-Dimensional Biomaterials

5a. CONTRACT NUMBER

5b. GRANT NUMBER
FA9550-14-1-0136

5c. PROGRAM ELEMENT NUMBER
61102F

6. AUTHOR(S)
Charles Lieber

5d. PROJECT NUMBER

5e. TASK NUMBER

5f. WORK UNIT NUMBER

7. PERFORMING ORGANIZATION NAME(S) AND ADDRESS(ES)
HARVARD COLLEGE PRESIDENT & FELLOWS OF
1350 MASS AVE STE 600
CAMBRIDGE, MA 02138-3846 US

8. PERFORMING ORGANIZATION REPORT NUMBER

9. SPONSORING/MONITORING AGENCY NAME(S) AND ADDRESS(ES)
AF Office of Scientific Research
875 N. Randolph St. Room 3112
Arlington, VA 22203

10. SPONSOR/MONITOR'S ACRONYM(S)
AFRL/AFOSR RTB2

11. SPONSOR/MONITOR'S REPORT NUMBER(S)
AFRL-AFOSR-VA-TR-2018-0365

12. DISTRIBUTION/AVAILABILITY STATEMENT
A DISTRIBUTION UNLIMITED: PB Public Release

13. SUPPLEMENTARY NOTES

14. ABSTRACT

The overall objective of this research is to develop nanoelectronic devices and macroporous mesh nanoelectronic networks for hybrid nanoelectronic/cell and cell network three-dimensional (3D) biomaterials. To this end, we developed an ultra-flexible syringe-injectable mesh nanoelectronics framework that can interface to biosystems with minimal chronic immune response, a novel multifunctional bioelectronic probe that can simultaneously record biomechanical and bioelectrical processes from the same cell, and free-standing nanoelectronic probes that can achieve highly localized electric field-based stimulation of primary neuronal cells. We have further developed this new paradigm of ultra-flexible syringe-injectable mesh electronics with the goal of exploiting the capabilities of targeting and recording from specific cell types or neuron subtypes. The natural distribution of both neurons and glial cells achieved post-implantation with tissue-like mesh electronics reported in Year 1 suggests that functionalization of recording and/or stimulation devices with antibodies or aptamers capable of recognizing and targeting specific cell surface receptors could enable in-vivo neuron subtype electrophysiology.

15. SUBJECT TERMS
nanotechnology, cyborg cell, nanoelectronics

16. SECURITY CLASSIFICATION OF:			17. LIMITATION OF ABSTRACT	18. NUMBER OF

Standard Form 298 (Rev. 8/98)
Prescribed by ANSI Std. Z39.18

DISTRIBUTION A: Distribution approved for public release.

a. REPORT	b. ABSTRACT	c. THIS PAGE		PAGES	19a. NAME OF RESPONSIBLE PERSON
Unclassified	Unclassified	Unclassified	UU		BRADSHAW, PATRICK
					19b. TELEPHONE NUMBER *(Include area code)* 703-588-8492

DISTRIBUTION A: Distribution approved for public release.

Final Performance Report – Years 1-4

Project Title:	Nanoelectronics Innervated Cells, Cell Networks and Three-Dimensional Biomaterials
Award Number:	FA9550-14-1-0136
Reporting Period:	06/15/2014 - 10/31/2018
Program Manager:	Dr. Patrick O. Bradshaw AFOSR/RTB2 875 North Randolph Street 4027 Arlington, VA 22203 E-mail: patrick.bradshaw.3@us.af.mil Phone: (703) 588-8492
Principal Investigator:	Professor Charles M. Lieber Department of Chemistry and Chemical Biology Harvard University 12 Oxford Street Cambridge, MA 02138 E-mail: cml@cmliris.harvard.edu Phone: (617) 496-3169

DISTRIBUTION A: Distribution approved for public release.

Final Technical Report – Years 1-4

Project Description and Objectives. Seamless merger of electronic devices with living biological systems could open up powerful opportunities in many areas, including monitoring of human physiology and enhancing human performance. The overall objective of this research is to develop nanoelectronic devices and macroporous nanoelectronic networks for hybrid nanoelectronic/cell and cell network 3D biomaterials. To achieve this broad objective we have pursued the following broad interdisciplinary areas. (1) Development of novel nanoelectronic devices for cellular communication, with an emphasis on nanostructures of a size scale similar to structures relevant to biological communication. (2) Investigation of communication between nanowire devices and living cells at the single-cell level, including elucidation of the limits for recording from and stimulating electrogenic cells, and exploring modulation of cellular activity. (3) Development of advanced macroporous nanoelectronic networks with high-yield arrays of nanowire devices for 3D innervation of cell networks. (4) Preparation of hybrid 3D nanoelectronic/cell networks and characterization of communication within and between such networks. We believe that the results of these studies have broken new ground and advanced our fundamental knowledge of how to build seamless nanoelectronic interfaces with individual cells through cell networks.

Summary. During the first year of the project we developed ultra-flexible macroporous nanoelectronics with rationally tunable mechanical properties and porosities that can be delivered in minimally invasive fashion through hollow needles via syringe injection. We demonstrated that these flexible nanoelectronics can unfold post-injection without damage to the electronic sensor devices in both man-made materials and living systems, as evidenced by unprecedentedly low or absent chronic immune response in live animal tissue. We showed that these novel nanoelectronics can enable multiplexed recording of acute and chronic neural activity, down to the level of single-neuron action potentials, with unparalleled stability. In the second year of this project we further developed novel bioelectronic probes for integrated into the previously developed framework for advanced bioelectronic interfaces, extending our work on injectable electronics to chronic measurements in freely behaving mice, and developed a novel approach to achieve spontaneous internalization of nanowires into neuronal cells. The third year of work saw the development of novel 3D bioelectronics probes that can achieve multifunctional bioelectronic interfaces by simultaneously recording biomechanical and bioelectrical processes from the same cell. We also demonstrated the ability to stimulate neurons using nanoelectronic devices that may be integrated into the previously developed framework for more advanced bioelectronic interfaces. The capability to locally excite cell membranes with sub-micron resolution represents a key advantage compared to traditional patch clamp method and optical stimulation techniques. We also developed a novel plug-and-play interface for the mesh electronics, opening the door to implementation of wireless technology in studies planned for the future. In the fourth year of this project we fabricated mesh electronics that incorporate this interface, and further extended the flexible syringe-injectable mesh electronics paradigm to exploit the capabilities of targeting and recording from specific cell types or neuron subtypes. The natural distribution of both neurons and glial cells achieved post-implantation with our tissue-like mesh electronics suggests that functionalization of recording and/or stimulation devices with antibodies or aptamers capable of recognizing and targeting specific cell surface receptors could enable in-vivo neuron subtype electrophysiology. Development of cell-targeting capabilities could open up broad new opportunities for electrophysiological tools, such as deconstruction of complex neural circuitry based on selective recording from specific subgroups of neurons.

DISTRIBUTION A: Distribution approved for public release.

YEAR 1

1. Design and demonstration of ultra-flexible macroporous mesh nanoelectronics. The mechanical properties of the free-standing mesh electronics are important to the integration with cells and cell networks, as well as the syringe injection process. The basic mesh structure **(Fig. 1)** consists of longitudinal polymer/metal/polymer elements, which function as interconnects between exposed electronic devices and I/O pads, and transverse polymer elements.

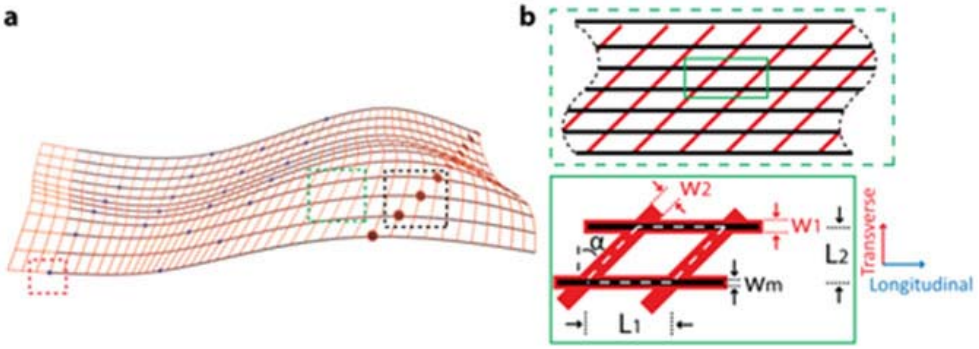

Fig. 1. a, Schematic of an injectable mesh electronics structure. The red-orange lines highlight the overall mesh structure and indicate the regions of supporting and passivating polymer mesh layers, the ca. horizontal black lines indicate metal interconnects between input/output (I/O) pads (black filled circles) and recording devices (blue filled circles). The red dashed box highlights two different types of devices - either electrochemical or field-effect transistors (FETs), the green dashed box highlights mesh network metal interconnects, and the black dashed box highlights I/O pads. **b**, shows a schematic (upper panel) of the zoomed-in region of mesh network highlighted by green dashed box in **a**, where black horizontal lines correspond to metal interconnects, red-orange lines highlight the transverse polymeric elements of the mesh. (Lower panel) corresponds to a single unit cell of the mesh (green box in upper panel) with the same color nomenclature as in (upper panel). The unit cell (white dashed lines) is defined by the following parameters: L_1 and L_2 are the unit lengths in the longitudinal and transverse directions, respectively; w_1 and w_2 are widths of the longitudinal and transverse mesh elements, respectively; and w_m is the width of metal interconnect lines.

The mesh longitudinal and transverse bending stiffness, D_L and D_T, are determined by the mesh unit cell and corresponding widths and thickness of the longitudinal and transverse elements, and the angle, α. Simulations of D_T and D_L versus α show that D_T (D_L) decreases (increases) for increasing α (**Fig. 2**). Hence, increasing α facilitates bending along the transverse direction (reduced D_T) and should allow for rolling up of the mesh electronics within a needle constriction, while at the same time increasing D_L, which reduces bending and potential buckling along the injection direction. Notably, the bending stiffness values for our nanoelectronic mesh are 10^5-10^6 times lower than for typical silicon, ultra-small carbon and 'flexible' polymer probes used for electrical recording from tissue, and represent a substantial advantage because of the importance of matching mechanical properties to avoid chronic tissue damage.

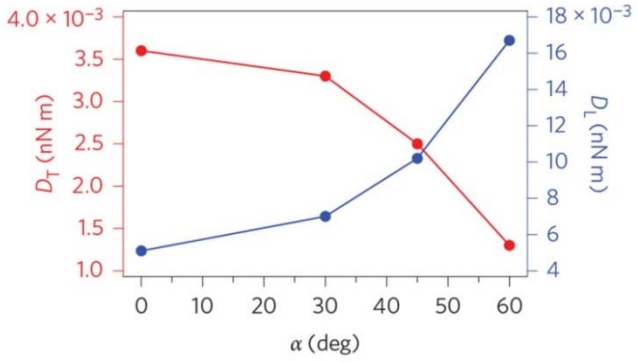

Fig. 2. Longitudinal mesh bending stiffness, D_L, and transverse mesh bending stiffness, D_T, as a function of α defined in **Fig. 1**.

DISTRIBUTION A: Distribution approved for public release.

The layout of key functional structures in the mesh electronics structure includes (i) sensor/stimulating elements at the end of the mesh electronics structure (dashed red box in **Fig. 1**), (ii) metal interconnects from sensor elements to the external connections (dashed green box in **Fig. 1**), and (iii) input/output (I/O) connections for external monitoring and control (dashed black box in **Fig. 1**). The capability to readily introduce different types of sensor/stimulating elements at positions designed for specific tasks represents a substantial strength of our approach.

2. Syringe injection of mesh nanoelectronics. To introduce the mesh electronics into needles, the tip end of a glass needle was connected to a syringe, and then the large end of the glass needle was used to suck the mesh electronics in towards the sharp needle tip. The correct orientation of the mesh electronics (i.e., recording devices at the needle tip) is readily achieved given visual asymmetry of the structures (**Fig. 3**). The needle was removed from the plastic tube/syringe and the large end connected to a conventional micropipette holder or syringe. A microinjector was then used to control the injection process, where the injection length per injector pulse or fluid low rate can yield well-defined ejection of the mesh electronics from the needles.

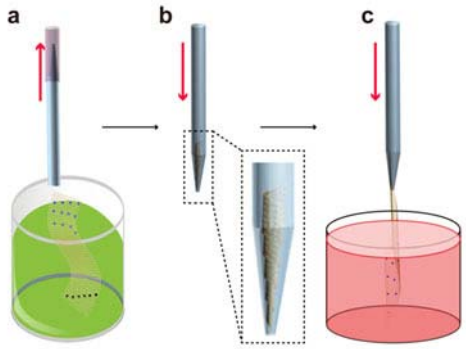

Fig. 3. Loading and injection of mesh electronics. a, The tip of the glass needle (blue) was connected to a syringe by a plastic tube (pink). The injectable mesh electronics (yellow) suspended in solution (green) was pulled into the needle from the large end of the glass needle such that the device end of the mesh enters the tube first. Black and blue dots represent the I/O pads and devices on the mesh electronics, respectively. **b**, The tubing was removed from the needle end and placed over the large end of the glass tube, and then the syringe was used to 'push' the mesh to the tip (inset, b). **c**, The glass needle was mounted in the x-y-z manipulator for injection into solution, gel/polymer or tissue (red). Red arrows indicate the direction of the fluid flow.

In **Fig. 4**, images of injection of a 2 mm wide sample through a 95 μm inner diameter (ID) glass needle show the compressed mesh ca. 250 μm from the needle opening, and then injected ca. 0.5 cm into 1x phosphate-buffered saline (PBS) solution. The 3D fluorescence image highlights the unfolding of the mesh structure from the point of the needle constriction (upper right). Higher-resolution images show that the mesh structure is continuous as it unfolds. Similar results were obtained for injection of a 1.5 cm width sample through a 20 gauge (600 μm ID) metal needle, demonstrating the generality of this injection through common glass and metal syringe needles.

DISTRIBUTION A: Distribution approved for public release.

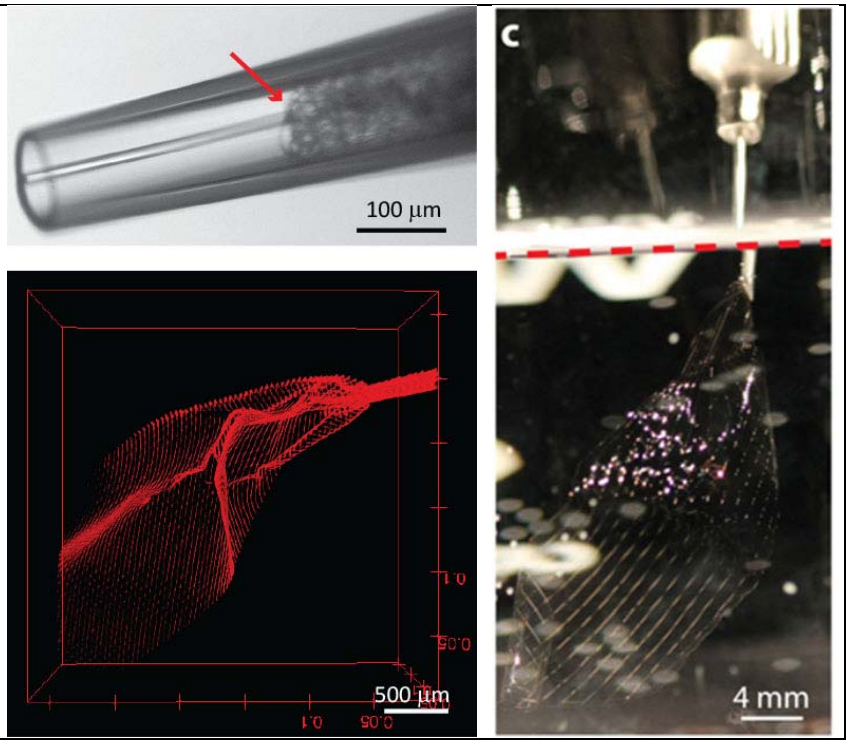

Fig. 4. Upper left: Mesh electronics immediately prior to injection into solution; the red arrow indicates the end of the mesh inside the glass needle. **Lower left**: 3D fluorescence image recorded following injection of ca. 0.5 cm mesh electronics into PBS solution. **Right**: Optical image of a 15 mm total width mesh electronics partially injected through a 20 gauge needle into PBS solution. The device end is fully unfolded at this stage of injection. The dashed red line corresponds to the air/solution interface.

We characterized the structures of different mesh electronics within glass needle-like constrictions to understand design parameters for successful injection (**Fig. 5**). Bright-field microscopy images of mesh electronics with different structural parameters recorded from the central region of different ID glass channels highlight two important features. First, mesh electronics with $\alpha = 45°$ and widths substantially larger than the constriction ID can be smoothly injected. Relatively straight longitudinal elements are seen in I and II, where the 5 mm 2D mesh widths are 11- and 20-times larger than the respective 450 and 250 µm ID needle constrictions. Second, even 1.5 cm width mesh electronics (III) can be injected smoothly through a 33-times smaller ID (450 µm) constriction. Corresponding 3D reconstructed confocal images with higher resolution of $\alpha = 45°$ mesh electronics samples with mesh width/constriction ID ratios from 11 to 33 (d, I to III) highlight several points. First, the longitudinal elements maintain a straight geometry without substantial bending through the constriction even for the 33:1 ratio (d, III). Second, these images show that the transverse elements bend with a curvature matching the needle ID, and the longitudinal elements and estimated number of rolls of the mesh at the needle constriction are comparable to geometric calculations. This latter point and further structural details were elucidated in cross-sectional plots of these images, which highlight uniformly organized transverse and longitudinal elements near the glass constriction IDs. Third, there is no evidence for fracture of $\alpha = 45°$ design mesh elements. Indeed, simulations of the strain versus needle ID show that the upper limit strain value for the mesh in a 100 µm ID needle, ~1%, is less than the calculated critical fracture strain.

DISTRIBUTION A: Distribution approved for public release.

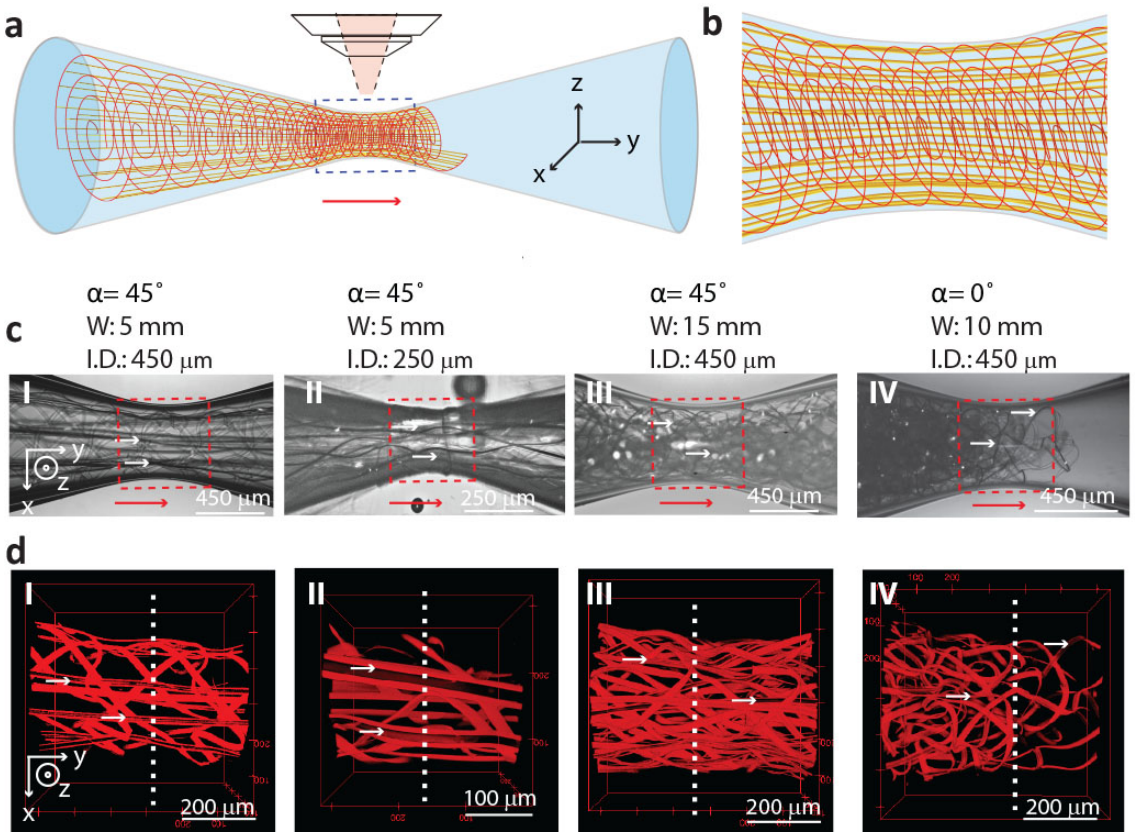

Fig. 5. a, Schematic illustrating the structure of a pulled glass tube (blue) with mesh electronics passing from larger (left) to smallest (center) ID of tube, where the red arrow indicates the direction of injection and x-y-z axes indicate coordinates relative to the microscope objective for images in **c** to **e**. **b**, Schematic image of the mesh structure from the region of the constriction indicated by the blue dashed box in **a**. **c**, Bright-field microscopy images of different design mesh electronics injected through glass channels. **I** and **II**, total width, W = 5 mm, α = 45° mesh electronics injected through 450 and 250 μm ID, respectively, glass channels. **III**, W = 15 mm, α = 45° mesh electronics injected through a 450 μm ID glass channel. **IV**, W = 10 mm, α = 0° mesh electronics injected through a 450 μm ID glass channel. The injection direction is indicated by red arrows in the images; the orientation relative to the axes in **a** are indicated in **I** and the same for panels **I** to **IV**.

In contrast, bright-field and 3D confocal images recorded from injection of α = 0° mesh electronics (c & d, IV) and thin-film electronics show that these structures are not smoothly injected through the needle-like constrictions. Specifically, images of a mesh sample with α = 0° (d, IV) but smaller width than α = 45° (d, III) exhibit jammed mesh at the constriction. The structure is deformed and fills the cross-section of the channel rather than rolling up as observed for α = 45°. Injection of thin film electronics with the same thickness and total width as the mesh in Fig. 2c, I for a width/needle ID ratio of 11 became jammed in the channel. Reducing the thin film width/needle ID ratio to 4 did lead to successful injection, although the 3D confocal microscopy images show substantial buckling of the structure in contrast to our α = 45° mesh design. These results confirm that the reduced transverse bending stiffness for the α = 45°design plays a key role in allowing the mesh electronics to smoothly roll up, follow the needle ID with minimum strain and thereby allow for injection of 2D widths >30 times the needle ID.

DISTRIBUTION A: Distribution approved for public release.

3. Post-injection properties of syringe-delivered mesh nanoelectronics. To test electrical continuity and functionality of the mesh electronics post-injection, we used anisotropic conductive film (ACF) to connect the I/O pads of the electronics post-injection to flexible cables that are interfaced to measurement electronics. Studies of the electrical performance and yield of devices following injection into 1x PBS solution through 100-600 μm ID needles highlight several points **(Fig. 6)**. First, metal electrochemical devices had an average device >94% and an

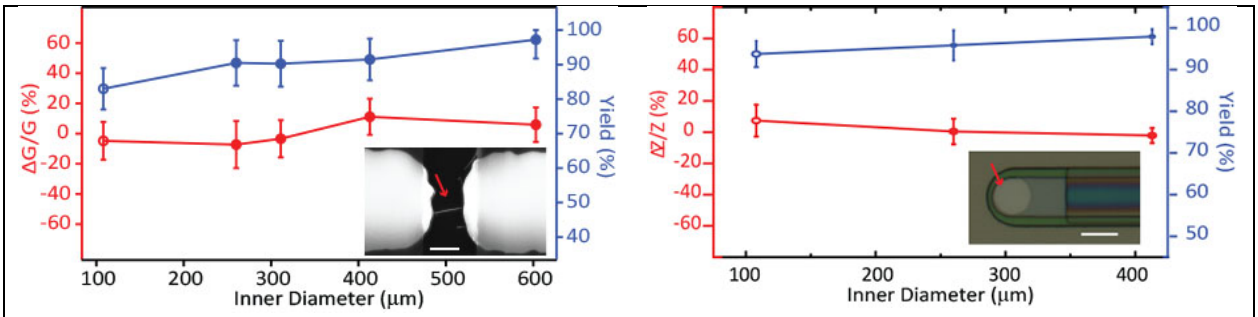

Fig. 6. Right: Yield (blue) and conductance change (red) of silicon nanowire FETs following injection. Inset: scanning electron microscopy (SEM) image of a nanowire FET device in the mesh electronics (red arrow). Scale bar: 2 μm. **Left**: Yield (blue) and impedance change (red) of the metal electrodes from the mesh electronics following injection. Inset: bright field image of a representative metal electrode on mesh electronics (red arrow). Scale bar: 20 μm.

average device impedance change, which represents an important characteristic for voltage-sensing applications, of <7% post-injection. Second, silicon nanowire field-effect transistor (FET) devices had a yield >90% for needle IDs from 260 to 600 μm, only dropped to 83% for the smallest 100 μm ID needles, and exhibited <12% conductance change on average post-injection. Together these results demonstrate the robustness of our mesh electronics design and the capability of maintaining good device performance following injection through a wide range of needle IDs.

Second, we investigated 3D gel structures without cavities as representative models of mesh electronics injection into biological tissue **(Fig. 7)**. Images recorded versus time following injection mesh electronics into Matrigel, a scaffold used in neural tissue engineering, have shown that the mesh unfolds ca. 80% in the radial direction over a 3-week period at 37 ºC. As expected, the degree of unfolding of the mesh electronics within the Matrigel depends on the gel concentration for fixed mesh mechanical properties with ca. 90% and 30% unfolding for 25% and 100% Matrigel, respectively. The ability to inject and observe partial unfolding of the electronics within gels with tissue-like properties also suggest that co-injection with other biomaterials and/or cells could be another application of injectable mesh electronics. Indeed, preliminary experiments show that co-injection of mesh electronics and embryonic rat hippocampal neurons into a matrigel leads to 3D neural networks with neurites interpenetrating the mesh electronics. Confocal images have shown the interpenetration between neurons and mesh structure of injectable electronics after co-injection into matrigel and culture for 14 days. These co-injection

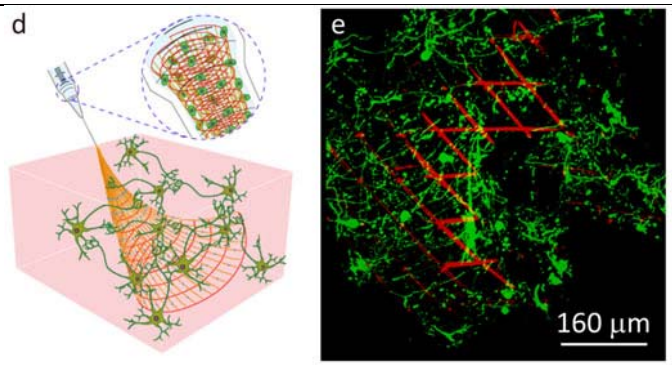

Fig. 7. d, Schematic of co-injection of mesh electronics & cells. **e**, 3D reconstructed confocal image; red and green colors correspond to SU-8 and β-tubulin, respectively.

results highlight potential opportunities for tissue engineering and stem cell therapy enhancements.

4. Chronic behavior of injected electronics in rodent brains. We have characterized the behavior of mesh electronics stereotaxically injected into the hippocampus (HIP) of live rodents, where the capability of delivering millimeters width electronics through 100's μm outer diameter (OD) needles allows for a much smaller window in the skull than the width of electronics, thereby reducing the invasiveness of surgery. Bright-field images of coronal tissues slices prepared 5 weeks post-injection (**Fig. 8**) demonstrate that the electronics is fully extended in the longitudinal direction. The mesh only relaxes a small amount with respect to the initial injection diameter (red dashed lines in image) given that the force to bend the mesh is comparable to the force to deform the tissue. In addition, an overlay of bright-field and DAPI epi-fluorescence images (right, image) show that the injection did not disrupt the CA1 and dentate gyrus (DG) layers of this region of the HIP. Notably, confocal images highlight unique characteristics of the injectable mesh electronics in dense neural tissue. First, analysis of GFAP fluorescence shows that there is a limited or an absence of astrocyte proliferation near the mesh, although the full image indicates a reduction in cell density at the central region of injection. Significantly, analysis of a similar horizontal slice samples prepared from three independent mesh injections also show limited or absence of astrocyte proliferation around our electronics, and quantitative analyses (**Fig. 9**) demonstrate that GFAP values versus distance from and along the mesh electronics surface are similar to background level. Second, these images show healthy neurons (NeuN signal) surrounding and close to the SU-8 ribbons of the mesh. Data and analyses from three independent samples support this observation quantitatively. Specifically, quantitative analyses demonstrate that the NeuN signals versus distance from and along the mesh electronics surface are enhanced or similar to background levels. These observations show the capability of the mesh electronics to promote positive cellular interactions, and are distinct from the chronic response of neural tissue reported for insertion of silicon, metal, flexible polyimide, and ultrasmall carbon electrical probes that exhibit reduced neuron density and enhanced astrocyte density near probes/tissue interface.

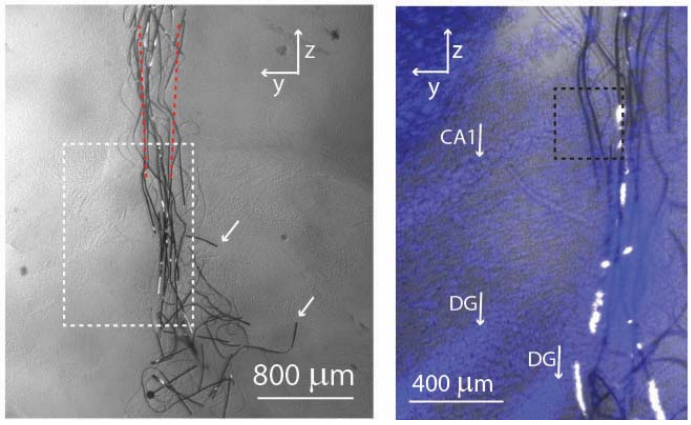

Fig. 8. **Left**: Bright-field microscopy image of a coronal slice of the HIP region 5 weeks post-injection of the mesh electronics at the position indicated in above schematic. Red dashed lines indicate the boundary of the needle, and white arrows indicate mesh elements broken during tissue slicing. **Right**: Overlaid bright field and epi-fluorescence images from the region indicated by white dashed box at left. Blue is DAPI staining of cell nuclei, white arrows indicate CA1 and dentate gyrus (DG).

DISTRIBUTION A: Distribution approved for public release.

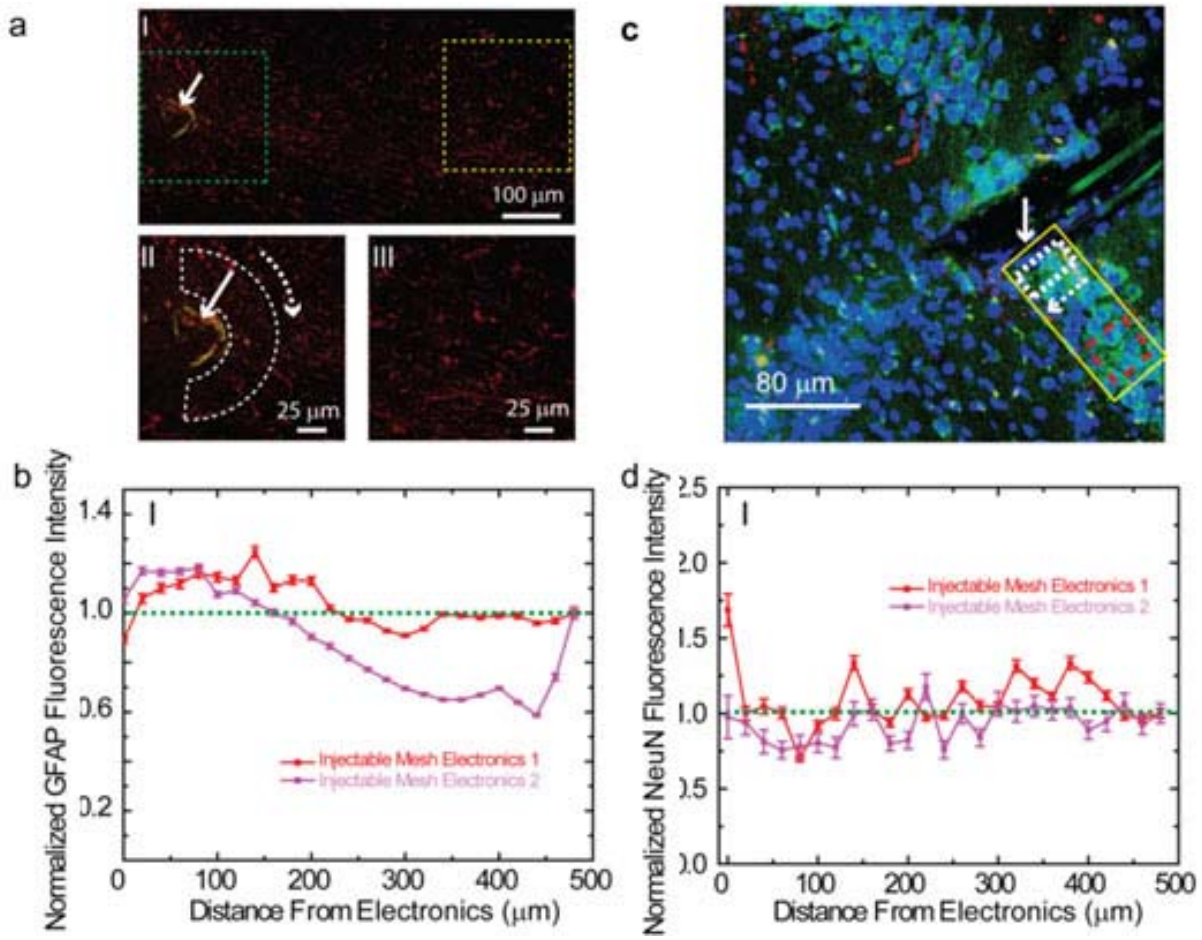

Fig. 9. a, Confocal microscopy fluorescence images of GFAP from injectable mesh electronics-1 sample. Red and yellow colors correspond to GFAP and SU-8 structures from mesh electronics, respectively. Solid white arrows highlight the ribbons from mesh electronics. II and III are zoomed-in higher resolution images corresponding to the green and yellow dashed boxes, respectively, in I. **b, I**, GFAP fluorescence intensities and standard error of the mean (s.e.m.) 4 weeks post-implantation versus distance from the interface of two different injected mesh electronics samples. The fluorescence intensity was normalized with the background value for each sample (value = 1, green dashed line) for comparison.

5. In addition, we have demonstrated the capability for electrical recording of neural activity with the syringe-injected mesh electronics by recording brain activity in the HIP of anesthetized mice following stereotaxic injection (**Fig. 10**). Representative multi-channel recording using

Fig. 10. Map of acute in-vivo mouse brain recordings from the HIP/cortex. The y-axis represents the depth beneath the brain surface of each sensor electrode, whose spatial distribution is specifically designed during fabrication. The x-axis shows the recording time. Colors indicate the amplitude of the recorded LFP amplitudes.

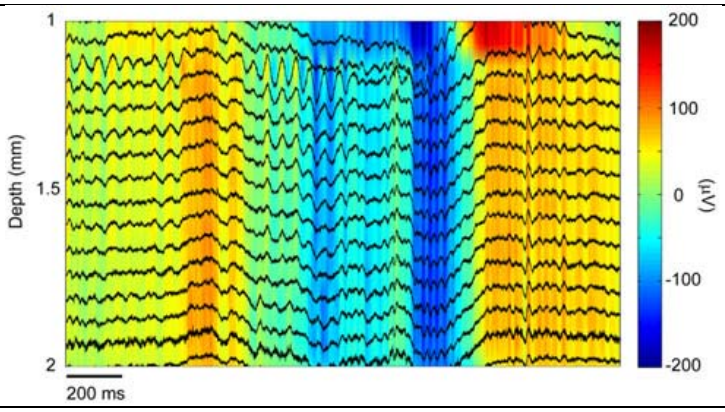

DISTRIBUTION A: Distribution approved for public release.

mesh electronics yielded well-defined signals in all 16 channels of the injected mesh. The modulation amplitude, 200-400 μV, and dominant modulation frequency, 1-4 Hz, recorded are characteristic of δ–wave local field potentials (LFPs) in the anesthetized/sleeping mouse. Moreover, spatiotemporal mapping of the LFP recordings (figure below) revealed characteristic hippocampal field activity for the rodent brain. In addition, standard analysis of sharp downward spikes showed a uniform potential waveform with average duration of ca. 2 ms and peak-to-peak amplitude of ca. 70 μV characteristic of single-unit action potentials. In the context of long-term chronic recording, our histology results and previous work demonstrate biocompatibility and long-term stability of using SU-8 passivated interconnects, and long-term stability of metal oxide passivated silicon nanowire sensors. Hence, we expect that these results together with the 'neurophilic' chronic response offer substantial promise for implantation and long-term brain activity mapping.

YEAR 2

1. Assembly and fabrication of 3D convex nanotransistors. Our 3D nanotransistor is created by translating a silicon nanowire across a thin height barrier (**Fig. 11**). The source and drain

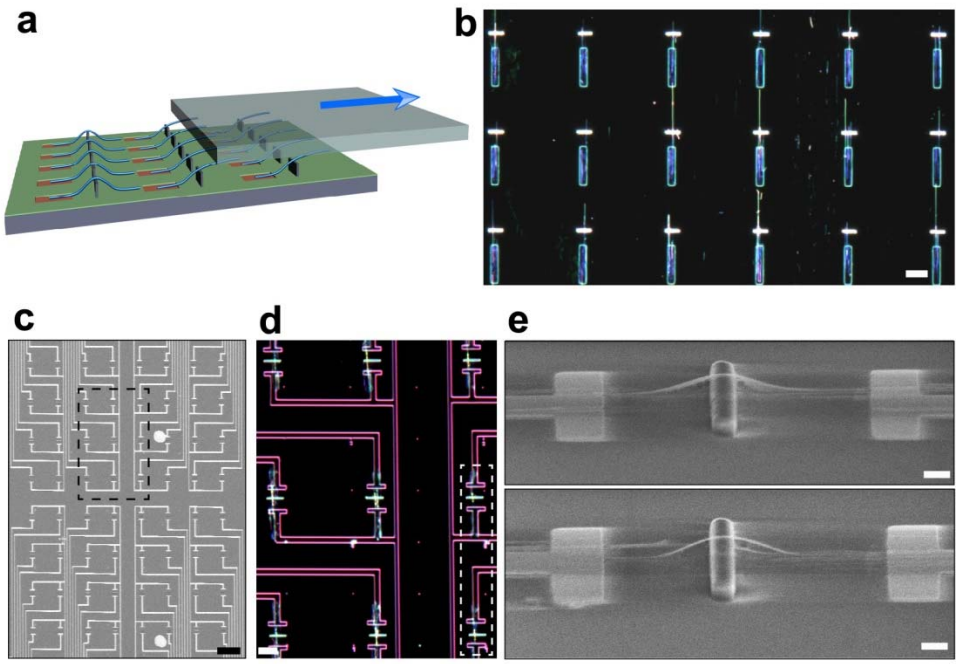

Fig. 11. a, Schematic of deterministic assembly of 3D convex nanowire structures, where one end of the nanowire is fixed by the anchoring window (red) and the remaining length is pulled over the height barrier by shear force from the translational motion (blue arrow) of the growth substrate. **b**, Dark-field optical image of an assembled 3×6 array. The bright horizontal bars and blue vertical windows indicate the height barriers and anchoring windows, respectively. Scale bar, 10 μm. **c**, Scanning electron microscope (SEM) image of fabricated 8×8 device array. Scale bar, 50 μm. **d**, Zoom-in optical image of a 3×3 device array corresponding to devices in the dashed box in (c). Scale bar, 10 μm. **e**, SEM images of two devices corresponding to the ones in the dashed box in (d). Scale bar, 1 μm.

contacts on the substrate and the height barrier supporting the apex of nanowire form a triangular or convex configuration, enhancing mechanical stability of the device. The 3D nanotransistor is constructed using a deterministic nanocombing technique invented in our laboratory and adapted in this work to 3D structures. First, arrays of narrow height barriers are lithographically defined. Then, arrays of anchoring windows (adhesive to nanowires) matching the height barriers are also

lithographically defined. Finally, nanowire growth substrate is brought into contact with the target substrate and translated along the length of the anchoring window. During the process, one end of the nanowire is first captured by the anchoring window, and the remaining length then pulled over the height barrier by shear force to form the convex structure.

The advances inherent in the assembly of the 3D nanotransistor include: (i) accurate positioning of individual nanowire structures at large (e.g., centimeter) scale, with (ii) uniform and controlled 3D geometry (0.8 μm high with 6.1 ± 0.7 μm spanning length). The capacity to control the positioning and geometry of a three-dimensional nanowire element represents a substantial leap from previous assembly methods, which only addressed nano-elements in planar configurations. (iii) The introduction of 3D geometric engineering adds new functionality.

2. Multifunctional sensing capabilities. The nanowire bending curvature yields an estimated maximum strain of ~0.3%, which is in the elastic region and far below the fracture limit. As a result, the 3D convex nanotransistor can serve as an electrical/chemical potential sensor based on the field effect in a conventional transistor, with a sensitivity to electrical potential of 2.4 ± 1.2 μS/V (characterized by the water-gate response in phosphate-buffered saline (PBS)) unaffected by bending and similar to those in unstrained planar nanowire transistors (**Fig. 12**).

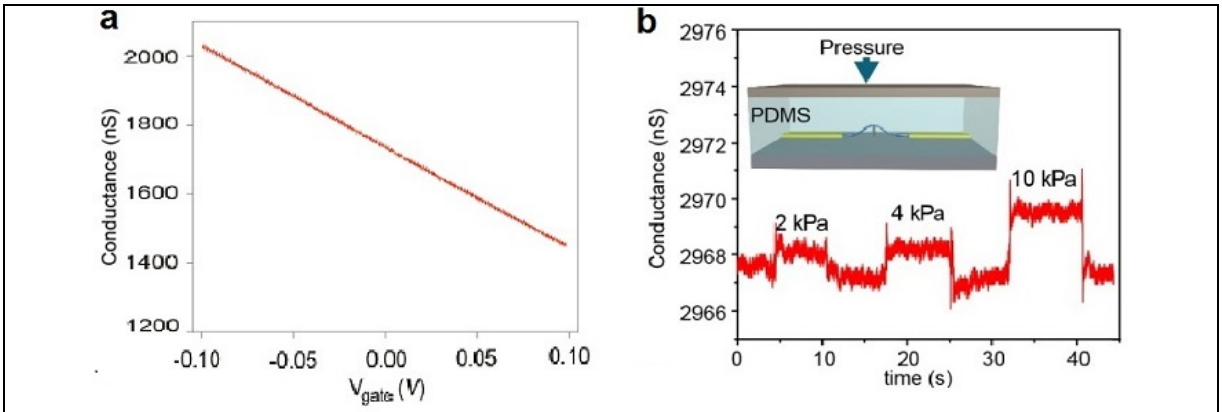

Fig. 12. a, Characterization of sensitivity to electrical potential in a typical device. The sensitivity or transconductance, *i.e.* the slope of the linear fit, is ~3.0 μS/V at zero V_{gate} in PBS. The data were recorded with V_{ds} = 0.1 V. **b**, Characterization of sensitivity to mechanical force. (Inset) The convex Si-nanowire devices are encapsulated by a layer of elastomer (polydimethylsiloxane or PDMS, 280 μm thick, 2 × 2 cm^2). The curve shows the conductance change with respect to different pressure loadings, with a pressure of 2 kPa clearly resolved. Such resolved pressure, based on simulation, is equivalent to a local force of ~17 pN along the axis of the nanowire.

Simultaneously, the geometric freedom and flexibility in the suspended nanowire "arms" allow for electrical detection of mechanical motion through the piezoresistive effect. Specifically, due to the giant piezoresistive effect unique to synthetic silicon nanowires, the 3D convex nanotransistor features ultrasensitive force sensitivity with an estimated detection limit of ~17 pN. This force is commensurate with the strength of a single bond in biomolecular interaction, and much smaller than typical cellular forces which range up to 100 nN. These two functionalities are bolstered by the structural uniformity and scalability in device assembly which enable the potential of multiplexed device arrays, and the 3D protruding geometry, which yields a tight interface with targeted biosystems for improved electrical and mechanical coupling.

3. Interfacing our 3D nanotransistor with cells to sense biomechanical and bioelectrical signals. The above structural and functional characterizations in the 3D convex nanotransistor indicate its potential as a cellular/subcellular multifunctional bioprobe for interrogating both biomechanical and bioelectrical properties (**Fig. 13**). For example, cellular motion can be

DISTRIBUTION A: Distribution approved for public release.

detected through the force-sensing capability in the device. Importantly, as opposed to detecting only the force normal to the device plane in planar sensors, here the quasi-1D nanowire in a 3D

Fig. 13. Schematic of nanowire-cell interface, where the convex silicon nanowire (navy blue) with source and drain contacts (yellow), is wrapped around by a cell highlighted with actin (red) and myosin filaments (cyan). Cell-contraction induced strain change causes local conductivity change (color gradient) in the nanowire. The right panel shows ion-flux induced local potential change that causes conductivity change (red pulse) in the nanowire during an action potential.

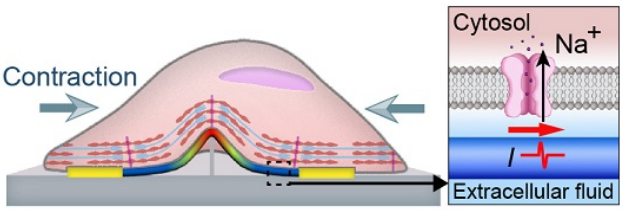

conformation allows multidirectional force sensing. Meanwhile, the electrical potential sensing capability enables probing of bioelectrical processes (e.g. action potentials) in cells. While biomechanical and bioelectrical processes can fall into to different frequency domains, both can be electronically detected and differentiated in this single device.

To demonstrate these capabilities, cardiomyocytes from neonatal rats were cultured on the device substrate (**Fig. 14**). Optical imaging reveals the apparent preference of cardiomyocytes for

Fig. 14. a, Confocal microscope image showing cardiomyocytes (green) preferably attached to the (yellow arrows) to the convex Si-nanowire devices. Scale bar, 20 µm. **b**, 3-channel multiplexed recording of cardiomyocytes. **c**, Zoomed signals from the black dashed box in (**b**). The stars indicate the positions of signals corresponding to action potentials. **d**, Zoomed signal from the red dashed box in (**c**), with Δt_1 the width of the broad signal, Δt_2 the time delay between the action potential and initiation of the broad signal. **e**, Superimposed action potentials as indicated by blue dashed box in (**d**). The red line represents the mean waveform for the single-unit spikes. **f,g**, Statistics for Δt_1 (N=22) and Δt_2 (N=22) as shown in (**d**).

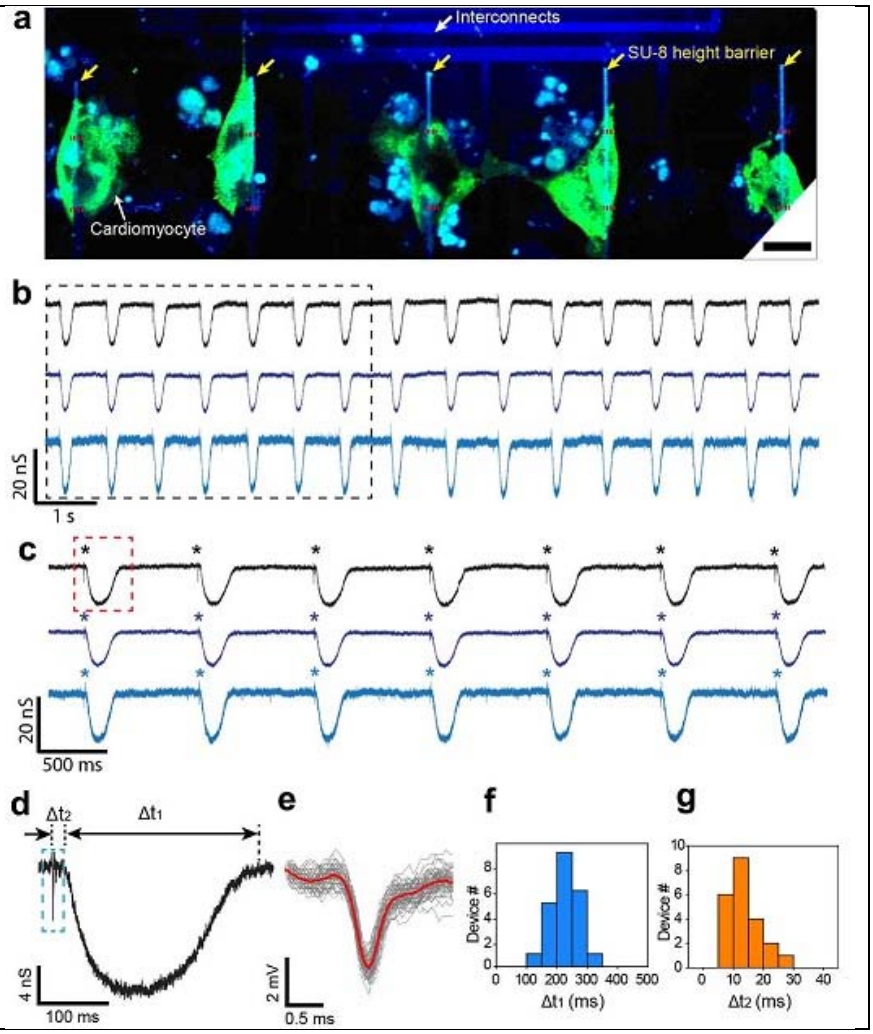

the device surface, possibly resulting from increased cell attachment to and proliferation on its convex 3D topology, and demonstrating a natural structural advantage for establishing a

DISTRIBUTION A: Distribution approved for public release.

bioelectronic interface with cells. The scalable device integration indeed enables multiplexed probing of cardiomyocytes. The frequency of the signals (~1.2 Hz) corresponds to the typical frequency of contraction (1-2 Hz) in rat cardiomyocytes. Specifically, each signal period includes two signals, with a sharp spike preceding a broader one. Standard analysis of the sharp spikes shows uniform potential waveforms with an average duration of ~0.5 ms and peak-to-peak amplitude of ~4 mV, characteristic of single-unit action potentials.

The origin of the broad spike coming from the mechanical motion of the cell is verified by the following observations First, the average width (~232 ± 46 ms) of the signal conforms to the time span of the contractile process in rat cardiomyocytes. Second, the shape or time evolution of the signal change, i.e. the rising and falling edges in the signal, is close to symmetrical, with a relatively slow slope (~100 ms), matching the length change in the sarcomere that governs cell contraction. Third, the average time delay (Δt_2 ~14 ± 6 ms) between signal initiation and action potential is consistent with the latency between action potential and release of Ca^{2+} from the sarcoplasmic reticulum that triggers the contraction in cardiomyocytes. Together, these results indicate that this broad spike arises from mechanical contraction in the cardiomyocyte.

This biomechanical signal is further verified by studying the correlation between the electrical recording and modulated cell contraction (**Fig. 15**). To this end, blebbistatin, a

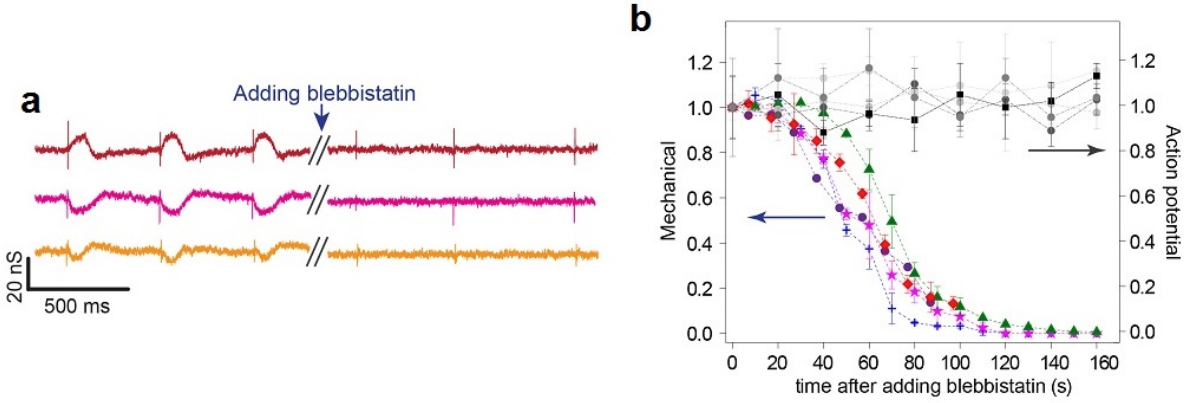

Fig. 15. Verification of biomechanical signals by blebbistatin tests. **a**, A 3-channel in-vitro recording in cultured cardiomyocytes before (left curves) and after (right curves) adding blebbistatin. **b**, Time evolution of normalized amplitudes of the biomechanical/broad signals (color curves, left Y axis) and action potentials (gray curves, right Y axis) after adding blebbistatin (N=5).

molecular inhibitor of myosin II, which is essential for motile machinery, was used to suppress cell contraction. Before blebbistatin is added, multiplexed recording from three devices shows synchronized broad-spike signals (~2.0 Hz) preceded by action potentials. After addition of blebbistatin (50 μM), the amplitude of the broad spikes gradually reduces to below the level of background noise, whereas the amplitude of the action potentials is maintained with similar frequency (1.9 Hz). The amplitude of the mechanical signal shows a uniform trend and reduces to below 20% in ~80 s. This signal decay is consistent with the decay profile (half-life <3 min) of sarcomere shortening and motion amplitude in rat cardiomyocytes perfused with blebbistatin. Meanwhile, the constancy of the action potential amplitude (gray curves, right Y axis) indicates the unaffected viability of other biological functions, consistent with the specificity of blebbistatin. Together, they reveal that the signal depression is exclusively correlated to suppression of cell contraction.

4. Biomechanical motion differentiation by 3D nanotransistor. The suspended nanowire arms enable force sensing from different directions, yielding different strain profiles that produce different electrical responses to reveal additional information regarding cellular motion. To

examine this, we first performed a simulation for the strain profile in a nanowire interfaced with a cardiomyocyte (**Fig. 16**). The simulation results indicate that the strain profile in the nanowire

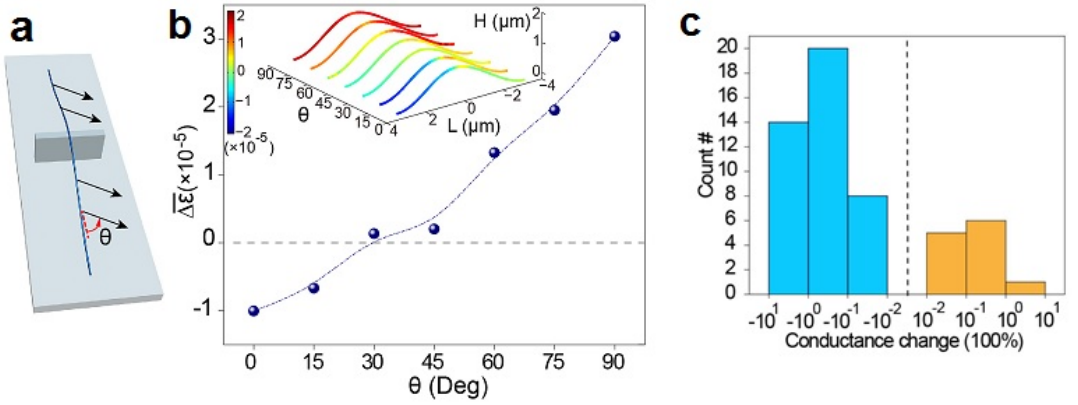

Fig. 16. a, Schematic of local cellular motion with respect to the axis of the nanowire, characterized by the in-plane angle θ. Due to structural symmetry, $0° \leq \theta \leq 90°$. **b**, Simulated average strain ($\Delta\varepsilon$) in the nanowire with respect to θ. The inset shows strain distribution along the nanowire at different angles. **c**, Distribution of sensing signs and amplitudes in mechanical signals. Out of 60 devices recorded from four different chips/batches, 42 (70%) had negative sign (conductance decrease) in the signals (blue columns), 12 (20%) had positive sign (conductance increase) in the signals (orange columns), and 6 (10%) showed mixed sign. The average conductance changes for the negative-sign and positive-sign signals were -0.86% (median -0.32%) and 0.22% (median 0.10%), respectively.

undergoes a transition from being dominated by compressive to tensile strain as the cell-nanowire interface angle θ increases from 0° to 90°. Specifically, a net compressive strain builds up in the nanowire for θ below ~26°; above this value the net strain becomes tensile. On the basis of random distribution, we predicted that a majority (71%) of the devices would experience tensile strain corresponding to a negative sensing sign. This expectation is consistent with our experimental observation that a majority of devices (70%) showed negative sensing signs. Meanwhile, the strain distribution yields average values of ~3.0×10^{-6} and -8.6×10^{-7} for tensile and compressive strain, respectively. These values correspond to the expected average conductance change of -0.45% and 0.13%, respectively. Again, this prediction is consistent with the experimental observation that negative- and positive-sign signals had average conductance changes of -0.86% (median -0.32%) and 0.23% (median 0.10%), respectively.

We further analyzed the correlation between electrical signals and cell motion by simultaneous optical imaging (**Fig. 17**). To this end, positions of nanotransistors were optically registered prior to cell culture. Cellular motion (e.g., amplitude and direction of local cellular displacement) was optically monitored and analyzed in specific device regions during a complete contractile process (7 frames, 314 ms) and compared with the simultaneous electrical signal recording, verifying that the cellular motion was faithfully reflected in the electrical recording. First, the amplitude in the electrical signal was shown to be proportional to the amplitude in cellular motion. Therefore, time evolution of the electrical signal can be used to reveal the time evolution in cellular displacement (**Fig. 17**).

DISTRIBUTION A: Distribution approved for public release.

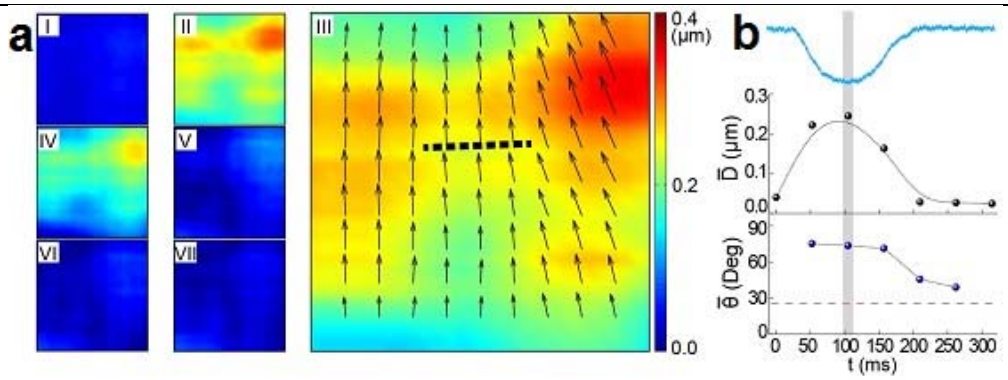

Fig. 17. a, Time evolution of local amplitude (color) and vector of cellular displacement corresponding to a 15×15 μm^2 cell area. The black dashed line indicates the position of the 3D nanotransistor. **b**, Correlation between electronic signal (top panel), average amplitude (D) (middle panel) and average angle θ (bottom panel) of cellular displacement at the nanowire region. Each data set (D, θ) corresponds to a frame in **a**. The dashed line indicates the threshold value of $\theta = 26°$.

In addition, the sign of the electrical signal correlates with the direction of cellular motion, as initially predicted by simulation. Experimental observations further confirmed this correlation. For example, a negative sign in the electrical signal indicates a cell-nanowire interfacing angle $\theta > 26°$, as verified above by optical imaging. Based on this, rotational cellular motion can be captured by a single nanotransistor probe, whose recorded electrical signal features a transition in the signal sign (**Fig. 18**).

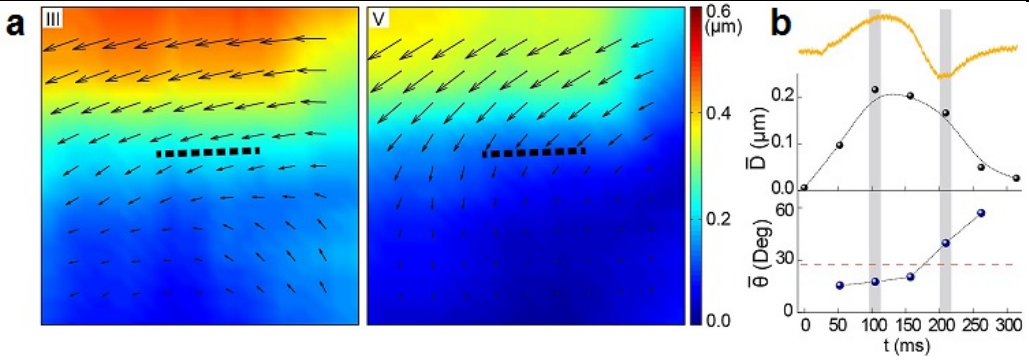

Fig. 18. a, Local amplitude (color) and vector of cellular displacement in a second cellular region at two time points. The black dashed line indicates the position of the 3D nanotransistor. **b**, Correlation between electronic signal (top panel), average amplitude (D) (middle panel) and average angle θ (bottom panel) of cellular displacement at the 3D nanotransistor region. The red dashed line indicates the threshold value of $\theta = 26°$.

In summary, this multifunctional nanotransistor bioprobe provides unique advantages. (i) Harnessing both functionalities in one device introduces an 'equivalent scaling' for device miniaturization necessary to minimize invasiveness. (ii) The spatial convergence of both functionalities enables in-situ probing of local dynamics involving bioelectrical and biomechanical interactions, which has been well demonstrated through simultaneous monitoring of excitation-contraction coupling in cardiomyocytes with high temporal resolution. Such temporal correlation can be indicative of diseases such as heart failure, whereas mechanical motion alone is relevant to various developmental processes. (iii) The integration of the devices on a large scale that is enabled by the deterministic assembly method pioneered here offers potential for multiplexing applications at bioelectronic interfaces.

DISTRIBUTION A: Distribution approved for public release.

5. Spontaneous internalization of cell-penetrating peptide-modified nanowires by primary neurons. In parallel with the efforts above, we are beginning work on a biomimetic approach that allows internalization of nanowires by primary neuronal cells without loss of cellular integrity or viability. This approach exploits a cell-penetrating peptide, the trans-activating transcriptional activator (TAT) from human immunodeficiency virus 1, which is known to penetrate the cell membrane and deliver materials of various sizes (ranging from angstrom to submicron) into primary cells and cell lines. These TAT peptides are conjugated onto Si nanowires and dispersed onto primary hippocampal cells. Live cell dynamic imaging (**Fig. 19**) shows that nanowire penetration begins 10–20 min after initial binding to the membrane, and

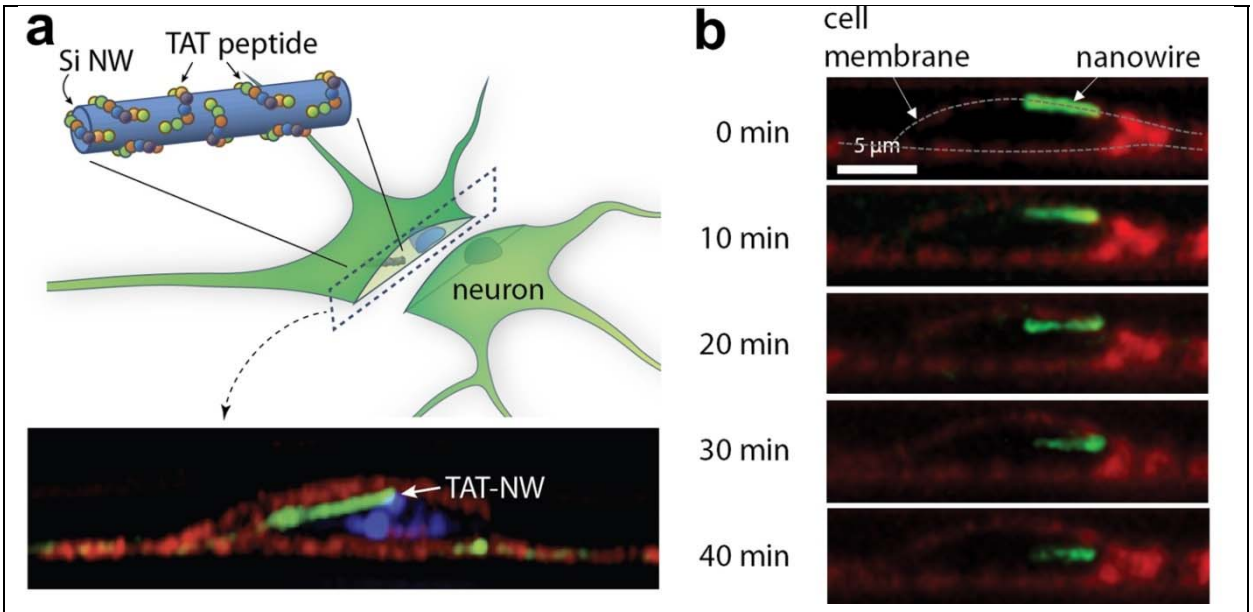

Fig. 19. a, Schematic (top) and confocal microscope image (bottom) of internalization of TAT peptide modified silicon nanowire into neuron. **b**, Live cell temporal cross-section confocal images of TAT-nanowire internalization into a neuron.

that nanowires become fully internalized within 30–40 min. Internalization is spontaneous and does not require mechanical or electrical assistance. The generality of this cell-penetrating peptide modification method is demonstrated by internalization of TAT-nanowires by primary dorsal root ganglion (DRG) neurons. These findings open up intriguing possibilities in intracellular recording from different primary neuron types using nano-bioelectronic devices.

6. Spontaneous chronic recording from freely behaving mice. Last, we have shown that mesh electronics can be directly bonded to a preamplifier (preamp) connector following injection to investigate chronic brain mapping from freely behaving mice. The lightweight interface is only 1.0 g with the preamp plugged-in (0.35 g without preamp), allowing data acquisition through a highly flexible cable that does not restrict animal motion (**Fig. 20a**). We also note that the overall interface has minimum impact on the animal while being housed without the preamp in the animal facility given its low profile and light weight. Representative single-unit spike recordings from five channels of mesh electronics five weeks post-injection (panel-b) are grouped into time periods when the mouse was whisking food (I) or foraging (II) in the novel cage environment. The two channels in the barrel field of the somatosensory cortex (Channels D & E) consistently show behavior-related firing rate increases during whisking with a return to baseline during foraging, while the other three channels exhibit no significant changes in firing pattern at 5, 10 and 27 weeks post injection (panel-c). Analyses of sorted spikes within the same recording sessions reveal stable unit isolation and dynamics of principle component cluster distributions as well as comparable fluctuations to the intrinsic recording noise level for each corresponding channel. Interestingly, phase locking analyses between single-unit firings in the

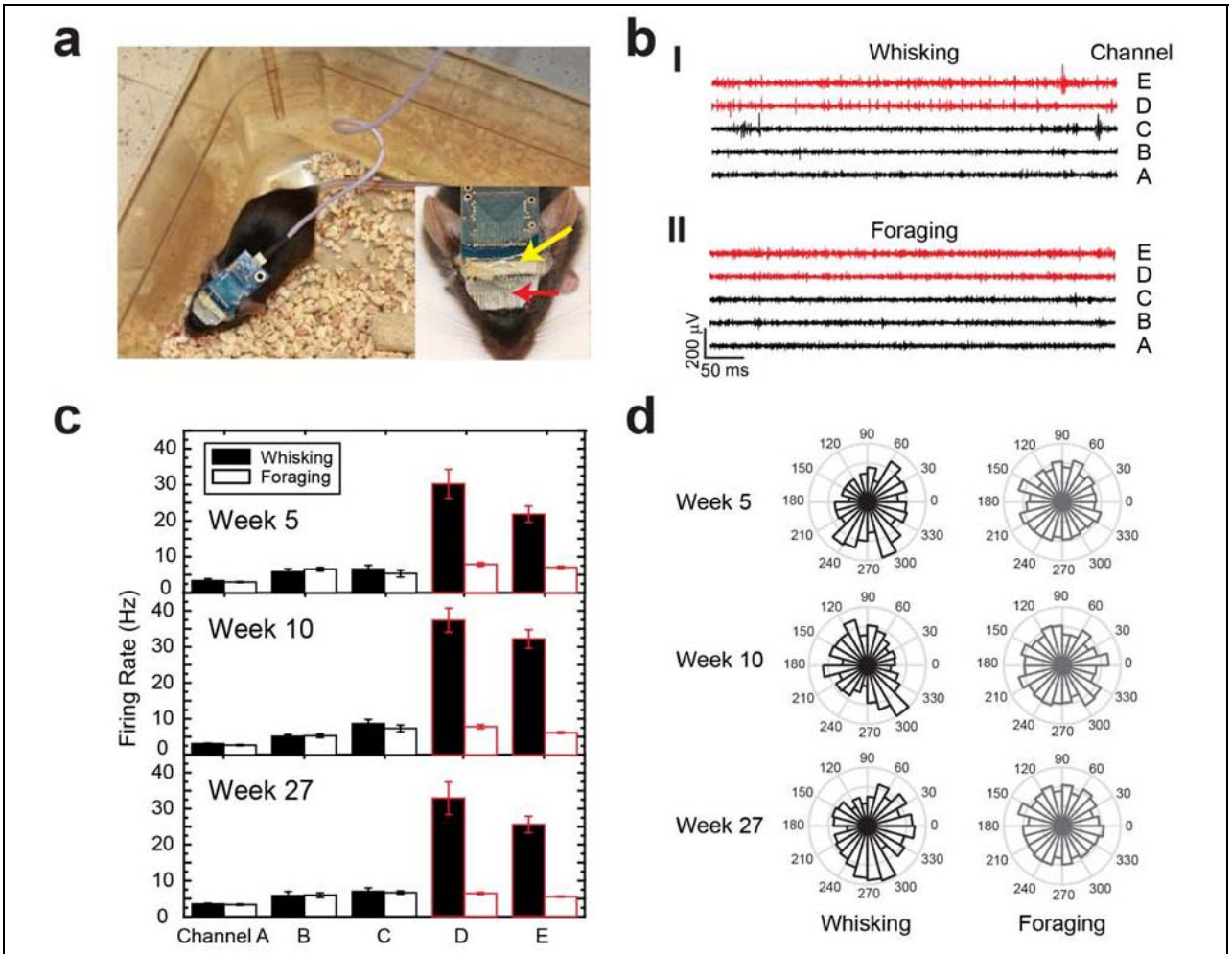

Fig. 20. a, Photograph of a typical freely behaving mouse recording A flexible serial peripheral interface (SPI) cable was used to transmit amplified signals to the data acquisition systems. Inset: A zoom-in view showing the conductive ink (black lines), FFC (red arrow), connector (yellow arrow) and the voltage-amplifier (blue-green rectangle). **b**, Single-unit spike recordings at 5 weeks post injection from five representative channels, two of which (Channels D & E, shown in red) are located in the somatosensory cortex, when the mouse was whisking food pellets (**I**) and foraging in the cage (**II**). **c**, Bar charts summarizing the changes in firing rate for the same five channels as shown in (**b**) during whisking (black bars) and foraging (white bars) at different times post-injection. The channels with whisking-associated neuronal responses are highlighted with red borders. **d**, Polar plots showing the phase-locking of single-unit spikes recorded in the cortex (Channel D) to the theta oscillations (4-8 Hz) in the hippocampus (Channel A) when the mouse is whisking and foraging.

barrel cortex (recorded by Channel D) and theta band local field potential (LFP) oscillations in the hippocampus (recorded by Channel A) at different time points indicate relatively constant phase-locking at ~300 degrees during active whisking motion versus no identifiable phase coherence during foraging (panel-d). These findings suggest the existence of an underlying pathway linking the barrel field of somatosensory cortex that receives vibrissa input and the hippocampus with higher-order processing of texture information.

YEAR 3

1. Transmembrane potential distribution in the localized electric field around p-i-n nanowires. We previously reported the synthetic integration of a p-n junction in the kinked

silicon nanowire structure, where the nanoscale p-n diode is naturally localized at the depletion region of the junction. In forward bias, the p-n nanowire can be used as a field-effect transistor (FET)-like localized voltage sensor for intracellular electrical recording. In this work, we show that the nanoscale p-type/intrinsic/n-type (p-i-n) junction, in reverse bias, can create a localized electric field sufficient to open voltage-gated ion channels in primary neuron cells and stimulate neuron activity. The p-i-n junction can be reverse-biased by applying negative voltage to the p-region and connecting the n-region to ground. In reverse bias below the breakdown voltage, there is no voltage drop at the junction; thus the p-arm is equipotential with negative charges. The native oxide layer serves as a parallel capacitor and prevents current flow between the nanowire and the solution. When the nanowire is brought in contact with the neuron membrane, the electric field localized at the nanowire surface can modulate the transmembrane potential and open voltage-gated ion channels such as sodium channels. This in turn can induce inward current and further depolarize the neuron, which might generate action potentials. The amplitude and localization of the electric field is readily controlled by the amplitude of reverse bias. If the p-i-n nanowire is reverse-biased by applying positive voltage to the n-region and connecting the p-region to ground, the electric field can instead hyperpolarize the cell and suppress neuron activity.

To examine whether the localized electric field around the p-i-n nanowire is sufficient to open voltage-gated ion channels, we used COMSOL finite-element-based electromagnetics solver to simulate the electric field generated by the reverse bias at the onset of the pulse and calculated the transmembrane potential in the membrane area in close contact with the nanowire. When the p-arm is biased at -2 V and the n-arm is grounded, the electric field distribution along the axial cross section of the nanowire confirms that the field that can create suprathreshold transmembrane potential localized around the p-arm (**Fig. 21a,b**). The radial cross section of the field shows that the membrane area at the interface with the nanowire can be depolarized above threshold; the affected membrane length at radial cross section is ~0.4 μm (**Fig. 21c,d**). Because the length of the p-type segment in contact with the cell membrane is <1 μm, the nanowire stimulation is highly localized, with submicron precision.

DISTRIBUTION A: Distribution approved for public release.

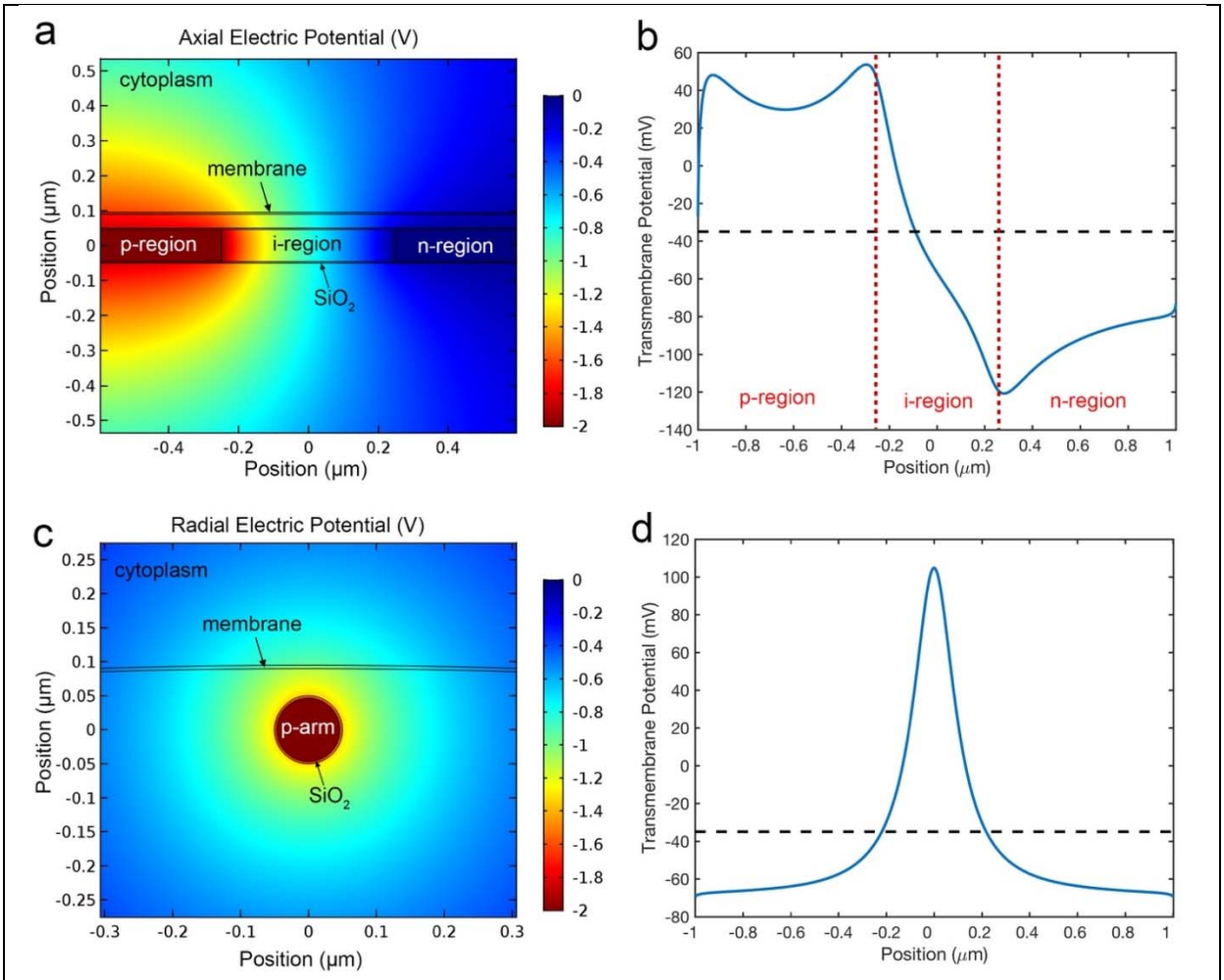

Fig. 21. Simulated transmembrane potential distribution in electric field surrounding the p-i-n junction. **a**, Electric field distribution along the axial cross section of the nanowire. Nanowire diameter: 100 nm (including 4 nm native silicon oxide); Cell membrane thickness: 5 nm; Minimum cleft between nanowire and cell membrane: 40 nm; Voltage applied to the p-region: -2 V. N-region is grounded. **b**, Transmembrane potential along the cell membrane calculated from (**a**). **c**, Electric field distribution along the radial cross section of the nanowire for the same parameters as in (**a**). **d**, Transmembrane potential along the cell membrane calculated from (**c**).

2. Design and characterization of p-i-n kinked nanowires. Recent work in our group has shown that nanotransistors can be synthetically encoded at the tips of kinked silicon nanowires. These kinked nanostructures can be readily configured as bioprobes, which allows us to record intracellular action potentials from beating cardiomyocytes in a minimally invasive manner. To achieve a highly localized interface between the p-i-n junction and the cell membrane, we have designed p-i-n kinked nanowires with the junction at the nanowire tip (**Fig. 22a**). The kinked nanowires are synthesized via gold-nanoparticle catalyzed vapor-liquid-solid (VLS) growth, with axial modulation achieved by switching dopant precursor gases, and growth direction switched by varying reactor pressure during elongation of the nanowire. Boron-doped p-type silicon nanowires are grown for 30 min, followed by 30 s growth of the intrinsic region. The reactor is evacuated for ca. 15 s to form the first kink, then growth is continued using phosphine dopant to create an n-type nanowire segment for 45 s, followed by a second cycle of reactor evacuation and continued growth using phosphine for ca. 30 min.

DISTRIBUTION A: Distribution approved for public release.

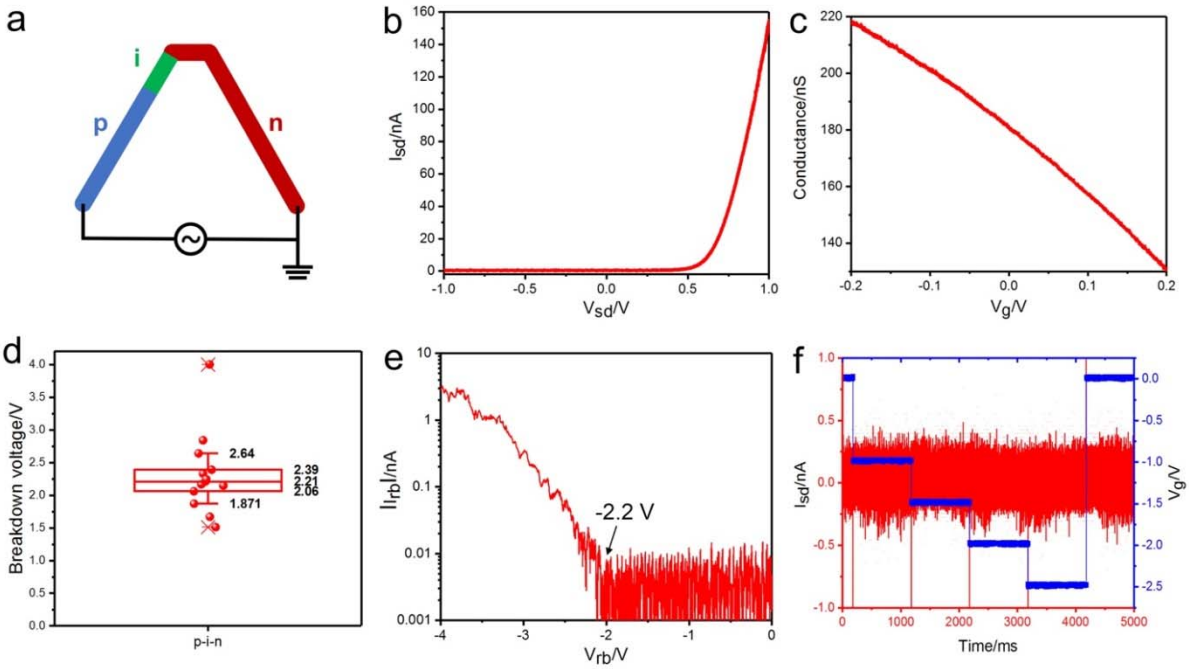

Fig. 22. Design and characterization of p-i-n kinked nanowires. **a**, Schematic of a kinked p-i-n nanowire with 60° tip angle. The blue, green and red lines designate the p-doped, intrinsic, and n-doped segments, respectively. **b** and **c**, Current versus voltage (I-V) data (**b**) and conductance versus water-gate voltage (V_g) data (**c**) recorded from a representative kinked p-i-n nanowire device. The p-i-n junction is forward biased at 1.0 V in (**c**). **d**, Box plot of the breakdown voltage in reverse bias. **e**, Reverse bias performance from a representative p-i-n nanowire. Black arrow indicates breakdown voltage at -2.2 V. **f**, Characterization of current leakage from metal contacts, where V_g is stepped from 0 V to -2.5 V. All experiments are carried out in Tyrode's solution.

Device characterization of the p-i-n kinked nanowires in Tyrode's solution demonstrated that current versus voltage (I-V) data show no measurable current in reverse bias and an onset for current flow at 0.6 V in forward bias (**Fig. 22b**). Representative conductance versus water-gate voltage (V_g) data demonstrate a p-type FET response and sensitivity of 225 nS/V (**Fig. 22c**). The average reverse bias breakdown voltage in Tyrode's solution is around -2.2 V, although this number can reach -4 V in some nanowires (**Fig. 22d,e**). No measurable leakage current from metal contacts is recorded when V_g is stepped from 0 V to -2.5 V (**Fig. 22f**), confirming that the metal contacts have no current leakage at the reverse bias voltages used in this work. The above measurements are performed before and after each neuron stimulation experiment.

3. Fabrication and assembly of 3D free-standing probes.

The p-i-n kinked nanowires are assembled onto the tip of free-standing probes. These probes can be manipulated in three dimensions to allow targeting of selected cells and/or subcellular regions on substrate or within tissue, and the release of probes from the fabrication substrate enables minimally invasive bioelectronic interfaces required for in-vivo measurements. Fabrication of free-standing kinked nanowire probes is carried out as follows (**Fig. 23a**). First, kinked nanowires with synthetically encoded p-i-n junction at the tip are deposited on a silicon wafer coated with sacrificial layer and SU8 photoresist passivation layer (**Fig. 23b**). Second, standard photolithography and e-beam lithography techniques are used to register the positions of individual nanowires and pattern the SU8 probe base (**Fig. 23c**). Third, gold source and drain electrodes are deposited on both arms of the kinked nanowire, followed by a top SU8 passivation

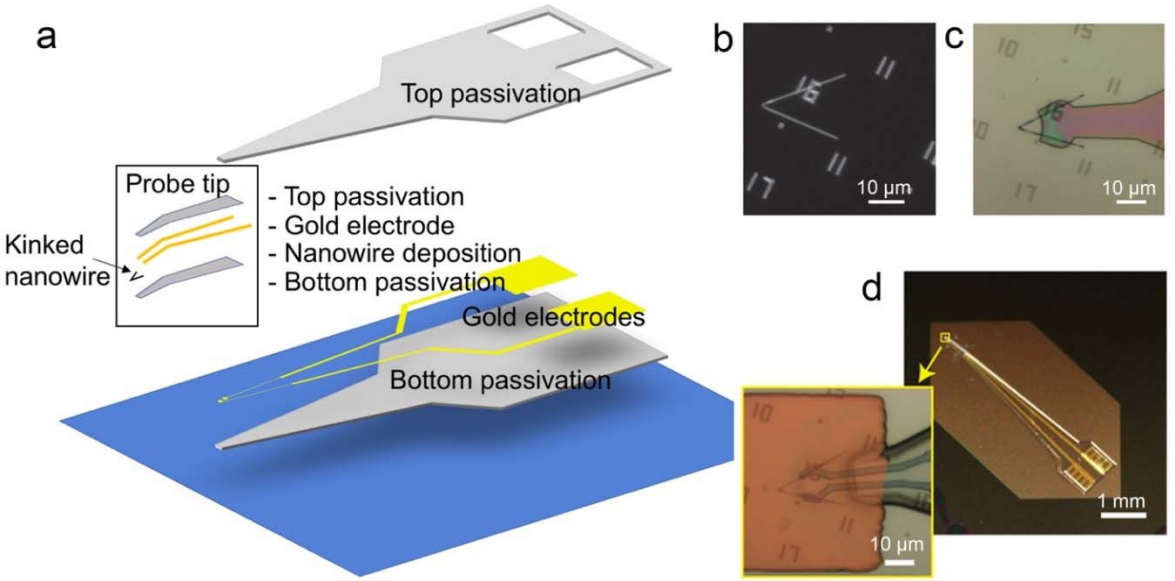

Fig. 23. Fabrication and assembly of free-standing nanowire probes. **a**, Schematic of the fabrication process of the free-standing probe, where the SU8 passivated gold electrodes serve as source and drain connections to the kinked nanowire. The inset shows zoom-in view of the probe tip consisting of a kinked nanowire sandwiched between the top and the bottom SU8 passivation layers. **b**, Dark-field image of a kinked nanowire on top of the SU8 layer. **c**, Bright-field image of the tip of the free-standing probe showing the kinked nanowire and the underlying patterned SU8 probe base. **d**, Digital camera image of a fabricated probe. The inset shows a bright-field image of the probe tip covered with a photoresist protection layer.

layer. Fourth, a photoresist protection layer is defined to cover the entire kinked nanowire (**Fig. 23d**). This layer prevents nanowire breakage during lift-off from the substrate. Finally, the probe is released by etching the sacrificial layer and assembled onto a printed circuit board, which can be mounted on a XYZ micromanipulator to target the selected cells cultured on glass coverslips.

4. Neuron stimulation using p-i-n nanowires. We used free-standing p-i-n nanowire probes to target and stimulate DRG cells, and whole-cell patch pipettes to record the intracellular electrical signals (**Fig. 24a**). Prior to measurements, the photoresist protection layer on the kinked nanowire is removed in solution. Intracellular recording is first established with a patch pipette in the whole-cell current-clamp mode with no injected current, and then the kinked nanowire probe is brought into contact with the cell membrane to form an inward 'dimple'. A differential interference contrast (DIC) image shows the kinked nanowire probe tip and patch pipette targeting the same cultured DRG cell (**Fig. 24b**). Reverse bias step at -2 V with 500 ms duration is applied to the p-i-n device to activate the ion channels on the membrane. The membrane potential, nanowire source-drain current, and voltage applied to the nanowire are simultaneously recorded before, during, and after stimulation (**Fig. 24c**). Note that the reverse bias voltage is slowly ramped down to -2 V in 50 ms to avoid capacitive peaks induced by sharp onset of the voltage step, and to exclude the possibility of stimulation by capacitive coupling. These data exhibit several key features. First, an action potential is induced at the beginning of the stimulation window, which is consistent with the response of DRG cells rich in tetrodotoxin-sensitive (TTX-S) sodium channels to current injection stimulation. Second, the resting potential of the cell is stable before and after stimulation, which shows that the cell membrane is not damaged during the process. Third, the nanowire current at forward bias is consistent before and after the stimulation window; no reverse bias leakage is observed during stimulation. Fourth, the

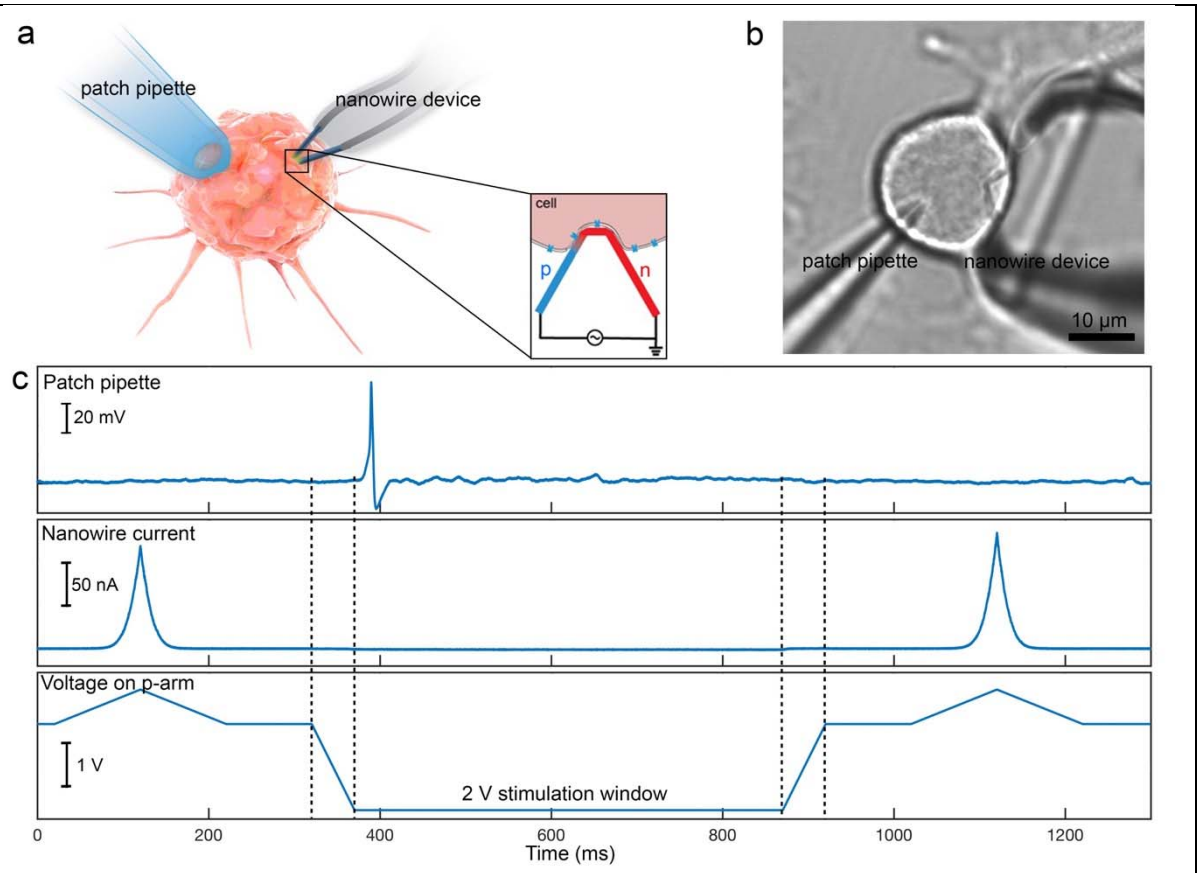

Fig. 24. Neuron stimulation using free-standing p-i-n kinked nanowire probe. **a**, Schematic of the experimental set-up. The patch-clamp pipette and nanowire probe are mounted on manipulators to target the same cell simultaneously. Neuron activity is recorded by the patch pipette during nanowire stimulation. The inset shows the cell membrane dimpling inward at the interface with the kinked nanowire tip. **b**, DIC image of the patch pipette and the kinked nanowire probe targeting the same cell. **c**, Top: Action potential recorded from the patch pipette; Middle: The p-i-n nanowire is characterized by forward bias before and after the stimulation window, and is reverse-biased at -2 V for stimulation; Bottom: Voltage applied to the p-type arm, while the n-type arm is grounded.

nanowire current at forward bias is not coupled to the patch pipette recording channel, which further proves that no current leaks from the metal contacts.

In addition, when negative current is injected through the patch pipette to hyperpolarize the cell, it shows depolarization in response to the same -2 V stimulation (**Fig. 25a**), confirming that nanowire stimulation cannot depolarize the cell to the firing threshold when hyperpolarizing current is simultaneously injected into the cell. Some DRG cells exhibit a high firing threshold. To examine the minimum nanowire voltage required for stimulation, we measured the current-clamp recording traces with stimulation amplitudes from -1.0 V, and -1.5 V to -1.9 V using standard reverse bias protocols (**Fig. 25b**). These data show the following key features: First, the reverse bias threshold of stimulation for this cell is between -1.0 V and -1.5 V. Second, stimulated depolarization amplitude increases with higher reverse bias amplitude, indicating a larger number of ion channels are opened at higher voltage. The inward ion current charges and depolarizes the cell. Third, the depolarization amplitude decays after reaching the peak, which is probably due to the opening of potassium channels and inactivation of TTX-S sodium channels. On another high-threshold DRG cell, we tested various depolarization durations in response to different stimulation waveforms at -2 V (**Fig. 25c**). The reverse bias voltage is held at -2 V for durations from 500 ms to 0 ms. Note that this cell does not show clear depolarization decay after

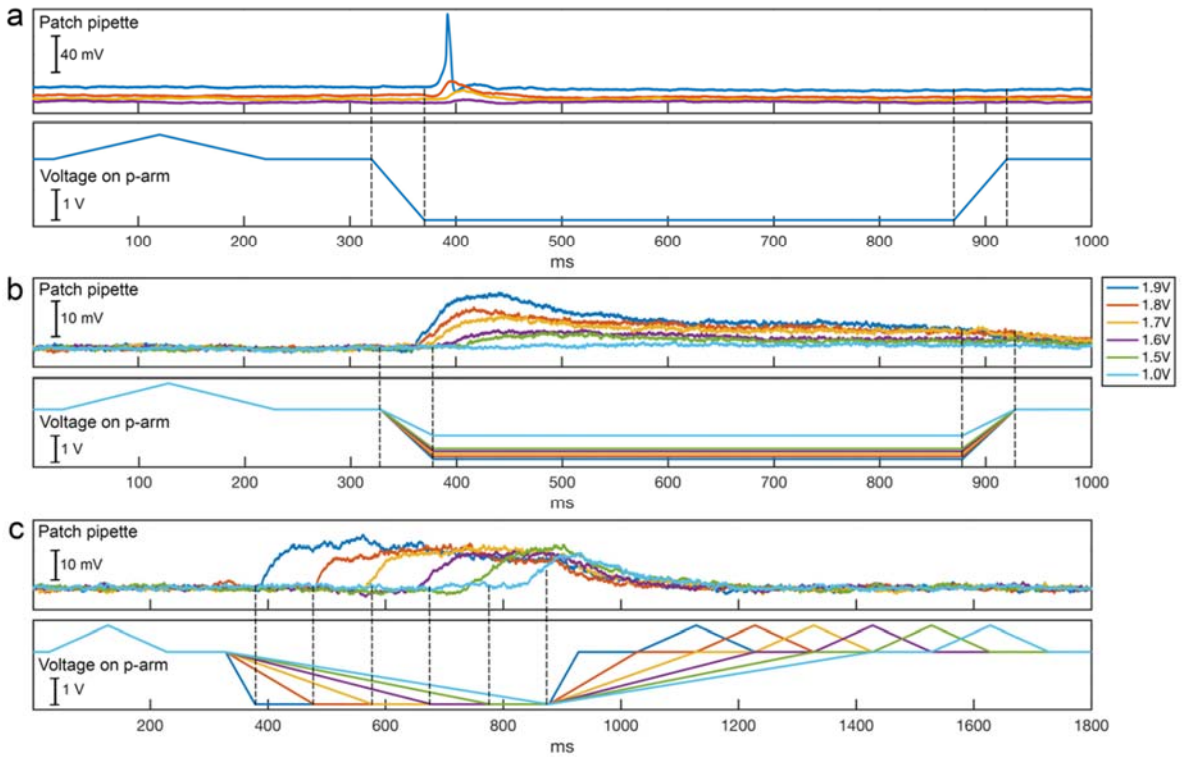

Fig. 25. Action potential and depolarization stimulated by p-i-n kinked nanowires. **a**, Action potential is recorded from the patch pipette upon nanowire stimulation at -2 V. The same cell shows depolarization in response to the same stimulation when the holding potential is hyperpolarized by the patch pipette. **b**, Different depolarization amplitudes recorded at stimulation voltages ranging from -1 V to -1.9 V. **c**, Different depolarization durations in response to different stimulation waveforms at -2 V.

reaching the peak, which might be due to the abundance of slow-inactivating tetrodotoxin-resistant (TTX-R) Nav1.9 channels.

In addition, some DRG cells show repetitive firing in response to sustained stimulation. These cells are believed to express a large number of Nav1.8 channels. The depolarized voltage dependence of inactivation of Nav1.8, together with rapid recovery from inactivation, allows repetitive firing with sustained depolarization. **Fig. 26** shows the response of one of this subclass

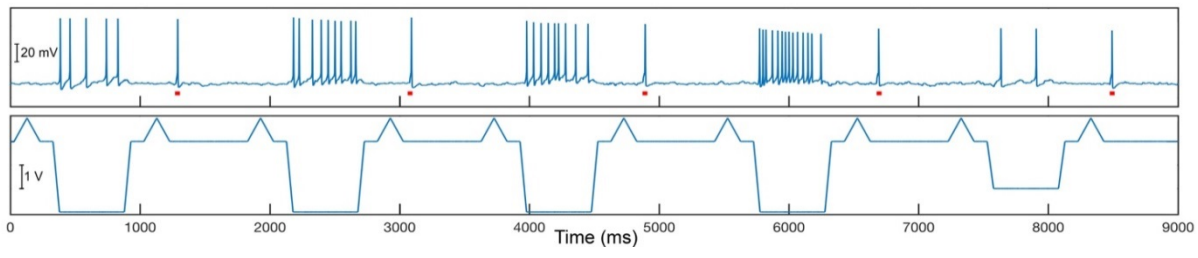

Fig. 26. Continuous firing from the same cell during -3 V and -2 V stimulation windows. The red dots denote pipette stimulation with 30 nA current injection.

of cells to reverse bias stimulation at both -3 V and -2 V. The cell fires continuously within the stimulation window, and shows higher firing frequency at -3 V than at -2 V.

In summary, this multifunctional nanotransistor bioprobe provides unique advantages. (i) Stimulation with conventional metal electrodes often produces Faradaic current, which leads to

electrochemical reactions on the electrode surface that can damage the cell membrane, and the patch clamp technique usually requires breaking through the membrane. In contrast, electric field-induced stimulation can be considered non-invasive as it avoids electrochemical reactions and does not damage the cell membrane. (ii) The highly localized electric field around nanowires enables membrane activation with sub-micrometer resolution. The ability to evoke local neuronal activity by isolating a single cell or subcellular area allows the study of neuron behavior with unprecedented precision. (iii) The convergence of both recording and stimulation functionalities demonstrates a more advanced bioelectronic interface for neuron manipulation. The ability to apply such localized stimulation opens up many exciting opportunities. For example, the ability to affect subtle details of neural firing while maintaining neural recording could be exploited for testing neural circuitry, as well as more general cellular networks. Furthermore, it has been shown that over time nano-stimulation of only one or a few cells has the potential to modify behavioral output. For brain-machine interfaces, using nanodevices for selective stimulation could allow the brain to remap different percepts. As such, we plan to aggressively pursue efforts to integrate these 3D nanowire-based bioprobe elements within the ultra-flexible mesh nanoelectronic framework for our ongoing and future in-vivo studies.

5. Three-dimensional imaging of syringe injected mesh electronics within neural tissue. Our previous studies of horizontal brain slices have provided detailed information about the local tissue/probe interfaces for the mesh electronics and flexible thin-film implants, allow comparison with previous studies of more rigid conventional probes, and have demonstrated the unique lack of immune response demonstrated by the mesh electronics for the first time in implant. These horizontal sections cannot, however, provide a global view of the probe/tissue interface, which typically extends millimeters in depth (e.g., in a mouse brain) or deeper in larger animals. As a step towards addressing this key issue we have recently developed a powerful approach for full-probe/tissue imaging (**Fig. 27**). Overall, the process involves making a sagittal brain section

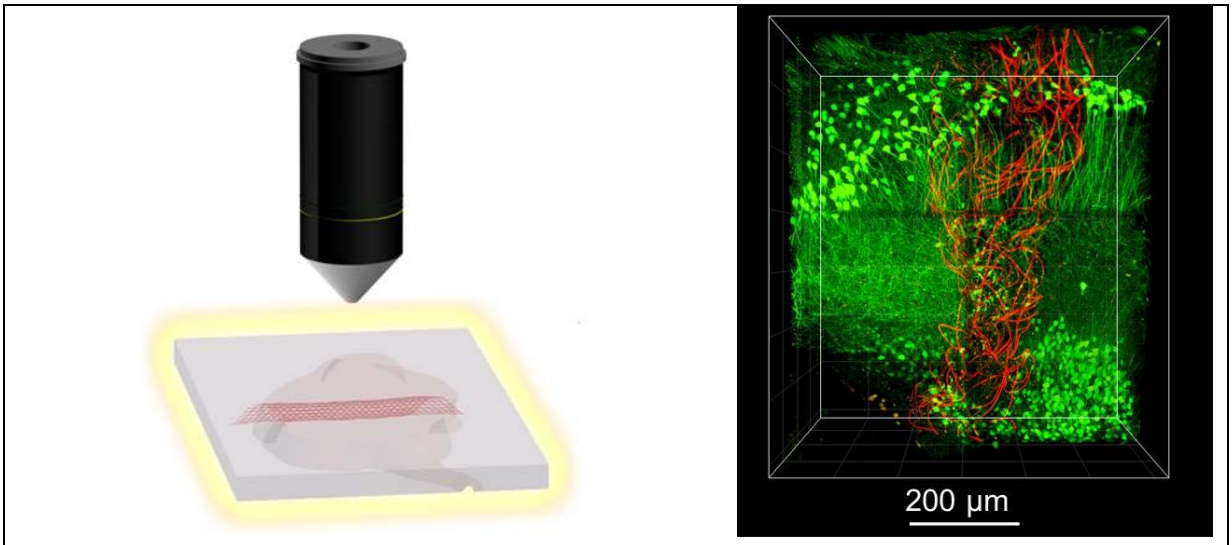

Fig. 27. Left: Schematic image of a thick sagittal tissue slice that includes the entire injected mesh electronics probe. **Right**: Confocal microscopy 2-photon image of the three-dimensional structure of the mesh electronics implanted within the hippocampus of a mouse. The mesh electronics was visualized by incorporating fluorescent label into the polymer structure by covalent chemistry during fabrication, and neurons correspond to YFP genetically-encoded indicator from a transgenic mouse.

parallel to the mesh electronics injection axis that contains the entire probe within the tissue slice, and subsequently imaging this relatively thick tissue slice. Several major challenges that had to be overcome to achieve this advance, include (i) imaging the whole brain with implanted mesh electronics by micro-computed X-ray tomography to define a reference surface parallel to the mesh long axis, (ii) vibratome sectioning of the oriented tissue to prepare tissue sections

containing the entire probe, (iii) optically clearing the relatively thick 0.5-2mm tissue sections to enable imaging through the entire sample, and (iv) staining relevant tissue and mesh structures for confocal fluorescence imaging. Notably, these initial studies demonstrate proof-of-principle capability for whole-probe imaging and thus open up many exciting opportunities for future work, including illumination of the full time-dependent tissue response in 3D following injection of the mesh electronics into the tissue, and the possibility (for the first time) of directly correlating the structure of a neural network with circuit activity.

6. Plug-and-play interface for the mesh electronics input/output (I/O). Last, we have developed a new syringe-injectable mesh electronics design with plug-and-play I/O interfacing that is rapid, scalable, and in general user-friendly to investigators. The underlying concept and implementation (**Fig. 28**) combines the in-vivo advantages of ultra-flexible mesh electronics

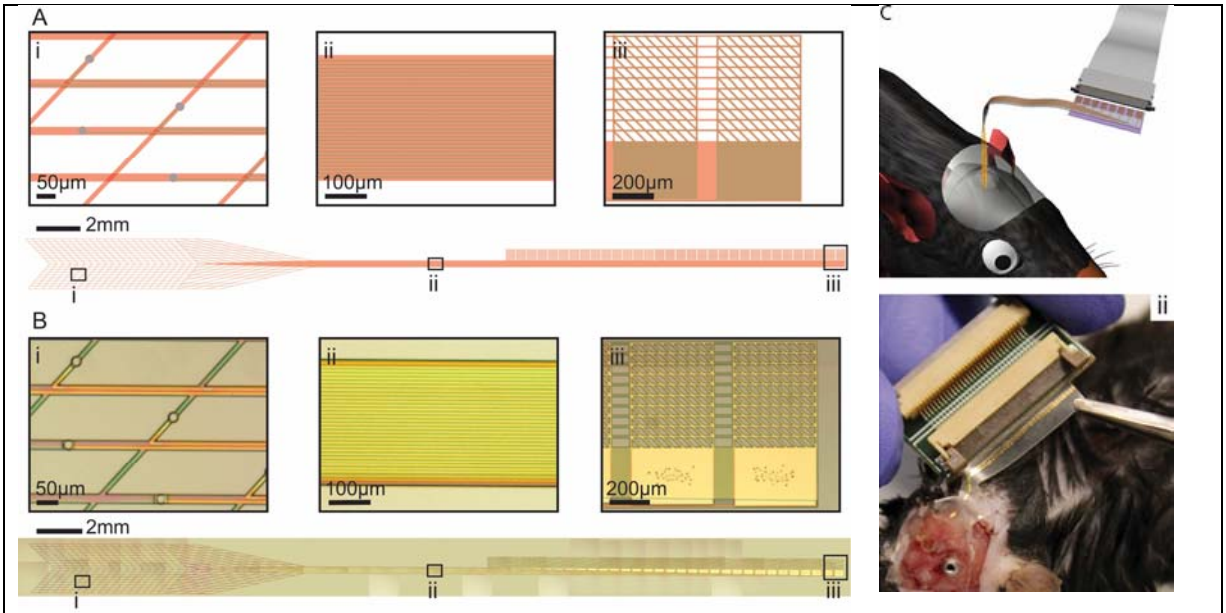

Fig. 28. Plug-and-play mesh electronics. (A) Schematic of syringe-injectable mesh electronics with plug-and-play I/O, with the ultra-flexible mesh device region at left tapering into the flexible stem and I/O regions at right. Insets provide magnified views of (i) recording electrodes embedded in the mesh device region, (ii) the solid SU-8 stem containing an independent metal interconnect for the devices, and (iii) the I/O pads. The pads shown here are 0.8 x 0.4 mm. (B) Bright-field optical microscopy images displaying the mesh electronics with plug-and-play I/O. (C) schematic (top) and experiment (bottom) showing insertion of the mesh I/O into a ZIF connector that is compatible with wired and wireless experiments.

with the convenience of what is typically a rigid I/O region of conventional probes. The stem, which transitions from the mesh region, is designed to fit without folding inside the injecting needle, while the I/O pads are made of conducting meshes with only the bottom side passivated by polymer so that they can roll up within the confined volume of the capillary needle during loading but then unfold to their full size once injected, enabling the use of I/O pads significantly larger than the diameter of the capillary tube. Importantly, the solid polymer stem is robust enough to be positioned with tweezers, and its stiffness precisely maintains the relative position of each I/O pad. The I/O pads are subsequently inserted into a zero-insertion-force (ZIF) connector mounted on a custom printed circuit board (PCB). Significantly, this new breakthrough will lower barriers for other scientists to utilize our mesh electronics and, moreover, facilitate our integration of the mesh electronics in wired and wireless freely-behaving experiments.

DISTRIBUTION A: Distribution approved for public release.

YEAR 4

1. Design and fabrication of mesh electronics. We have fabricated mesh electronics that incorporate the plug-and-play input/output interface (**Fig. 29**), as reported in Year 3. The design of the mesh region is similar to the ultra-flexible macroporous nanoelectronic framework that has demonstrated minimal chronic immune response and stable long-term tracking of individual

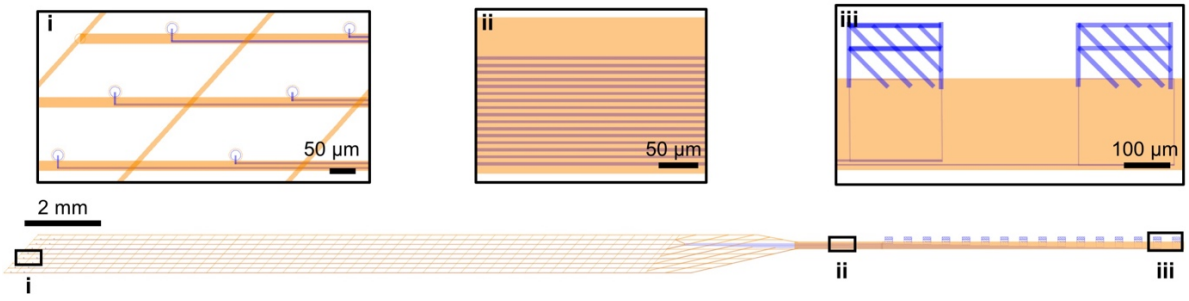

Fig. 29. Design of mesh electronics. Schematic of mesh electronics with plug-and-play I/O, with the ultra-flexible mesh device region at left tapering into the flexible stem and I/O regions at right. Insets provide magnified views of (i) recording electrodes embedded in the mesh device region, (ii) the SU-8 stem containing metal interconnects, and (iii) the I/O pads.

neurons in vivo, as reported in Year 1. The interconnect lines from the recording electrodes are routed into a stem region, and the input/output (I/O) region, where the I/O pads will be spread onto a flat flexible cable (FFC) connector for recording data acquisition. Fabrication of mesh electronics were carried out as follows. First, photolithography was used to define the bottom passivation layer of SU-8 polymer on a sacrificial layer. Second, gold (Au) interconnects and recording electrodes were deposited on top of the bottom SU-8 layer using in the second photolithography step. Third, interconnects were passivated with a top layer of SU-8 polymer, leaving the I/O pads and the recording electrodes exposed. Mesh electronics were released from the fabrication substrates by dissolving the sacrificial layer before loading into capillary tubes for injection.

2. Surface modification approaches for selective conjugation of antibodies on Au electrodes. To target and record from specific cell types or neuron subtypes using mesh electronics, we have developed two surface modification approaches for selective conjugation of antibodies on Au electrodes. In the first approach (**Fig. 30a**), hydroxyl-poly(ethylene glycol)-

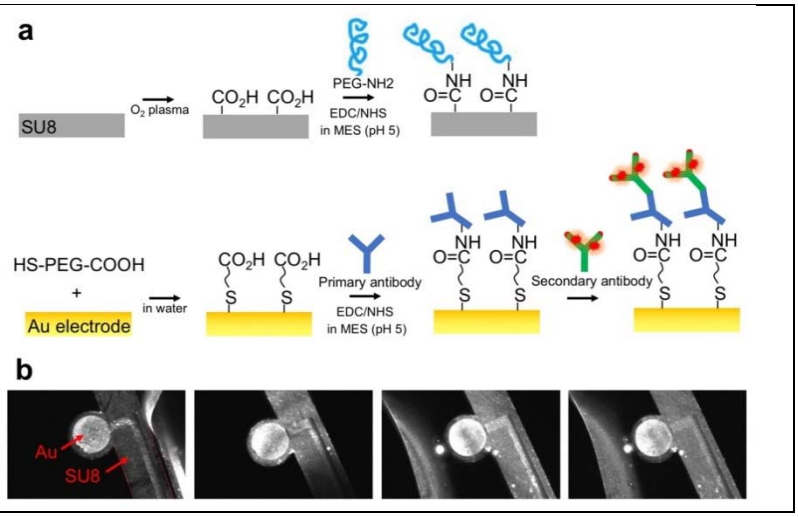

Fig. 30. Surface modification of electrodes on mesh electronics. **a**, Schematic of the modification steps, where SU8 is covered with PEG, and electrodes are modified with primary antibodies using EDC/NHS coupling, before labeled with fluorescent secondary antibodies for imaging. **b**, Confocal fluorescent images electrodes embedded in SU8 ribbons.

amine (HO-PEG-NH_2, molecular weight 5,000) was first covalently coupled to the carboxyl (-COOH) groups on oxygen plasma-treated SU8 polymer using 1-ethyl-3-(3-

(dimethylamino)propyl) carbodiimide (EDC) and N-hydroxysuccinimide (NHS) in 2-(N-morpholino)ethanesulfonic acid (MES) buffer (pH = 5) containing 0.5 % Tween 20. In this step, PEG coupling was utilized to modify the SU-8 surface to prevent the -COOH groups on SU-8 reacting with primary antibodies in the next step. The Au electrodes were modified using water-soluble thiol-PEG-COOH (HS-PEG-COOH, molecular weight 200) via gold-thiol bonds. The -COOH groups on the Au electrodes were then covalently coupled to $-NH_2$ groups on primary antibodies using EDC/NHS in MES buffer with Tween. The modification layer was characterized by incubating mesh electronics in secondary antibodies labeled with fluorophores and imaged using confocal fluorescence microscopy. The increased fluorescence on the Au electrodes over the PEG-modified SU8 indicates that the antibodies can be selectively conjugated onto Au electrodes (**Fig. 30b**).

In the second approach (**Fig. 31a**), click chemistry reagents thiol-PEG-azide (molecular weight 235) and dibenzocyclooctyne-sulfo-N-hydroxysuccinimidyl ester (DBCO-sulfo-NHS) were first mixed and incubated overnight, before conjugating $-NH_2$ groups from primary antibodies to -NHS and adding 0.5 % tween 20. Mesh electronics were then incubated in the mixture, before labeling with secondary antibodies and imaging using confocal fluorescence microscopy. **Fig. 31b** shows that incubating azide-DBCO-modified antibodies with the mesh electronics enables the antibodies to selectively label the Au electrodes with minimal binding to the SU-8.

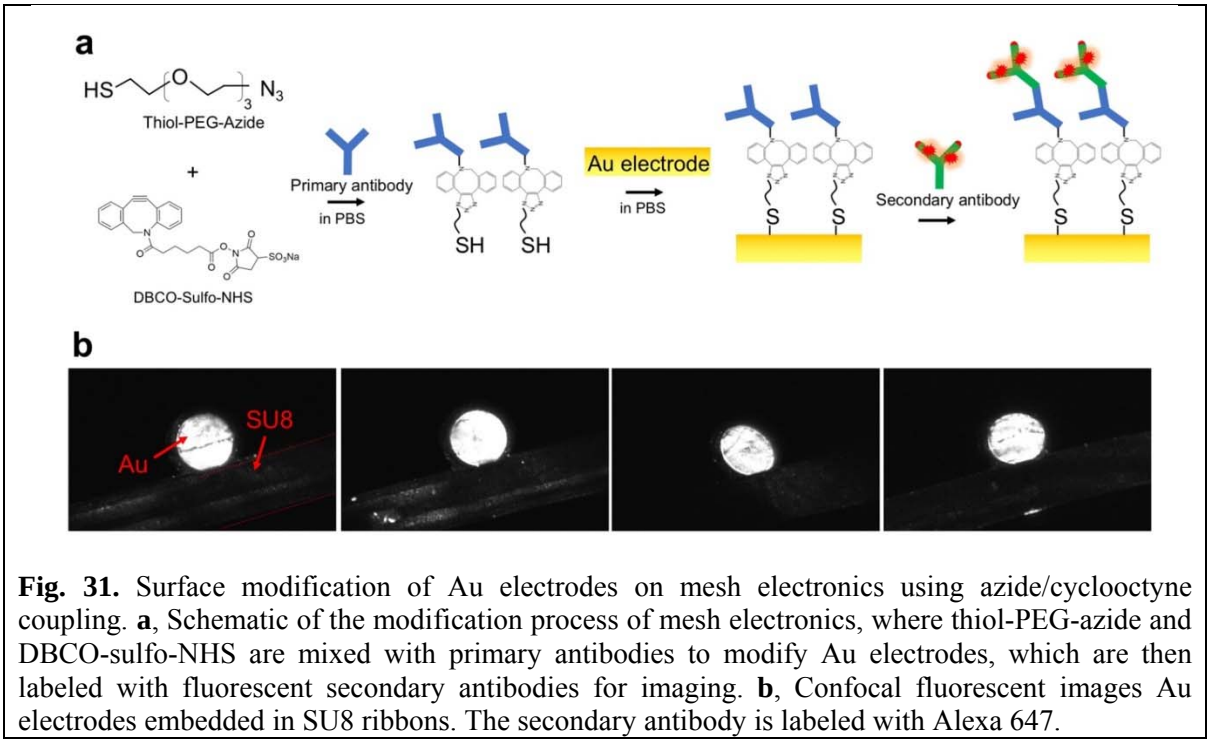

Fig. 31. Surface modification of Au electrodes on mesh electronics using azide/cyclooctyne coupling. **a**, Schematic of the modification process of mesh electronics, where thiol-PEG-azide and DBCO-sulfo-NHS are mixed with primary antibodies to modify Au electrodes, which are then labeled with fluorescent secondary antibodies for imaging. **b**, Confocal fluorescent images Au electrodes embedded in SU8 ribbons. The secondary antibody is labeled with Alexa 647.

In summary, we have fabricated mesh electronics that incorporate the plug-and-play input/output interface and developed two surface modification approaches for selective conjugation of antibodies on Au electrodes. We believe the development of cell-targeting capabilities of mesh electronics could open up broad new opportunities for electrophysiology tools. As such, we plan to aggressively pursue efforts to modify the mesh electronics with antibodies for targeting specific cell types (e.g., neurons and microglia cells) or neuron subtypes (e.g., dopaminergic neurons) in ongoing and future in-vivo studies.

DISTRIBUTION A: Distribution approved for public release.

CURRENT AND FUTURE WORK

1. Preliminary results: Wireless recording of freely behaving rodents. Until recently, all of our recording has been limited to studies of restrained and/or 'wired' moving mice, which has made investigations of freely-behaving animals for studies of learning and neural plasticity difficult. Recently acquired equipment from Deuteron Technologies has now been installed and enables multi-channel (16, 32, and 64) wireless recording and stimulation of mice to realize the potential of the unprecedented recording and stimulation stability afforded by injectable mesh electronics. The system can be connected to a mouse implanted with one or more mesh electronics via a specially designed printed circuit board that is mounted on the mouse head. A computer remotely communicates with the system to initiate and monitor recording of electrophysiology data to an on-board Micro-SD memory card directly attached to the wireless equipment. Recording can proceed for up to two hours without disruption, which is sufficiently long to perform many behavioral tasks related to memory and learning.

Initial tests show that using a wired commutator, which is the standard approach used in wired experiments to allow for motion of the animal subject without twisting of the connection cable, to record electrophysiology significantly inhibits the ability of mice to freely roam in both open-field and y-maze tasks (**Fig. 32**). The turning of the commutator reduces the wire tension and enables mice to behave more freely than they can without it, but frequent untangling is still necessary to allow the mouse brief periods of 'free' movement.

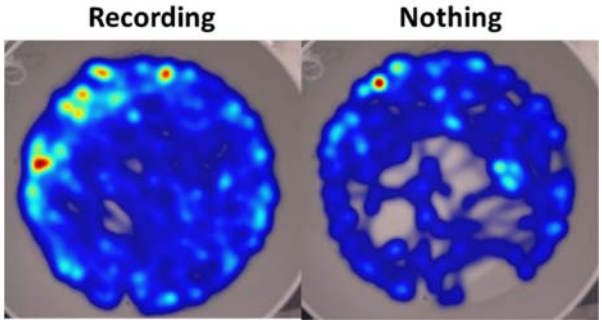

Fig. 32. Mouse exploration in an open field task. Representative heat map for the locations of a single mouse during 10 minutes with the wireless recording equipment (left) followed by 10 minutes exploring without the wireless recording equipment (right). The wireless equipment did not diminish the mouse's exploration with similar results for 4 separate mice.

In addition, these same mice are able to freely move with the wireless recording equipment, with no sign of inhibited mobility or exploration in y-maze tasks (**Fig. 33**). Thus, this wireless equipment will enable investigations of chronic electrophysiology in freely-behaving animals.

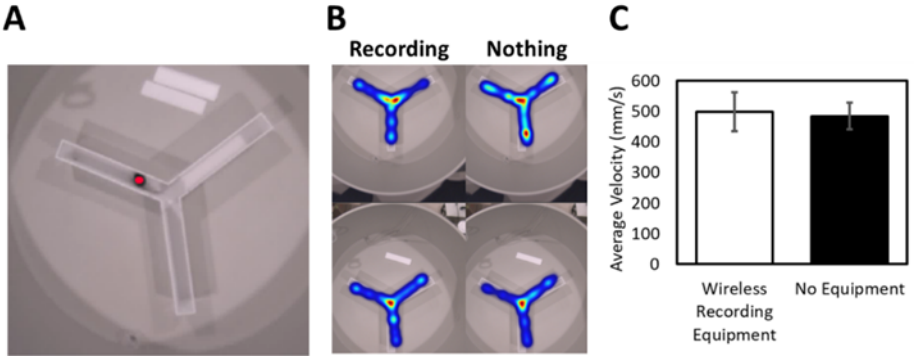

Fig. 33. Mouse exploration in Y-maze. Representative mouse during 4 consecutive 5-minute trials in a Y-maze alternating between exploration with and without the wireless recording equipment. **a**, The animal is tracked using a mounted camera and Noldus Ethovision XT software. **b**, The wireless equipment did not diminish the mouse's exploration in alternating trials. **c**, The velocity of the mouse was no different with and without the wireless recording equipment.